

2

DTIC FILE COPY

Technical Report  
815

# Measurements of Tilt Anisoplanatism at the Firepond Facility

AD-A202 681

DTIC  
SELECTED  
JAN 25 1989  
DC

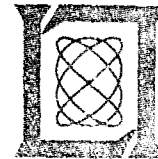
R. Teoste  
J.A. Daley, Jr.  
R.N. Capes, Jr.  
J.J. Alves  
M.D. Zimmerman  
A.V. Roberts

18 November 1988

**Lincoln Laboratory**

MASSACHUSETTS INSTITUTE OF TECHNOLOGY

LEXINGTON, MASSACHUSETTS



Prepared for the Department of the Air Force  
under Electronic Systems Division Contract F19628-85-C-0002.

Approved for public release; distribution unlimited.

REPRODUCED FROM  
BEST AVAILABLE COPY

The work reported in this document was performed at Lincoln Laboratory, a center for research operated by Massachusetts Institute of Technology. This work was sponsored by the Air Force Weapons Laboratory under Air Force Contract F19628-85-C-0002.

This report may be reproduced to satisfy needs of U.S. Government Agencies.

The views and conclusions contained in this document are those of the contractor and should not be interpreted as necessarily representing the official policies, either expressed or implied, of the United States Government.

This technical report has been reviewed and is approved for publication.

FOR THE COMMANDER

*Hugh L. Southall*

Hugh L. Southall, Lt. Col., USAF  
Chief, ESD Lincoln Laboratory Project Office

Non-Lincoln Recipients

**PLEASE DO NOT RETURN**

Permission is given to destroy this document  
when it is no longer needed.

MASSACHUSETTS INSTITUTE OF TECHNOLOGY  
LINCOLN LABORATORY

MEASUREMENTS OF TILT ANISOPLANATISM  
AT THE FIREPOND FACILITY

R. TEOSTE  
M.D. ZIMMERMAN  
Group 55

J.A. DALEY, JR.  
R.N. CAPES, JR.  
J.J. ALVES  
Group 52

A.V. ROBERTS  
Group 76

TECHNICAL REPORT 815

18 NOVEMBER 1988



Accession For	
NTIS CRASI	<input checked="" type="checkbox"/>
DTIC TAB	<input type="checkbox"/>
Unannounced	<input type="checkbox"/>
Justification	
By	
Date	
Author	
Title	
Dist	
A-1	

Approved for public release; distribution unlimited.

## ABSTRACT

Tilt anisoplanatism is the atmosphere-induced differential tilt seen by a common telescope observing two light sources separated by a very small angle. This report summarizes the results of tilt anisoplanatism measurements made at the Firepond Facility in Westford, Massachusetts. Two very precise visible quad trackers were used to simultaneously track each component of selected binary stars whose angular separations were in the range of 47 to 107  $\mu\text{rad}$ . While the report describes the tracking hardware and its characterization, the major contribution of this work is quantifying the tilt anisoplanatism under a variety of seeing conditions. The measurements showed that the magnitude of tilt anisoplanatism can be on the order of 1- $\mu\text{rad}$  rms for a 1.2-m telescope, a value several times larger than previously believed. The frequency distribution of the differential tilt is extremely variable, but most of the jitter strength lies below 30 Hz, with almost negligible contributions above 100 Hz. Calculations of the tilt anisoplanatism magnitude were made by the Optical Sciences Company using the SLC and Hufnagel-Valley turbulence models. The calculations are in general agreement with the measurements, but accurate predictions require precise atmospheric measurements as inputs to the models.

## TABLE OF CONTENTS

Abstract	iii
List of Illustrations	vii
List of Tables	ix
1. INTRODUCTION AND SUMMARY	1
1.1 Historical Background	1
1.2 Experimental Equipment	2
1.3 Summary of Results	3
2. EQUIPMENT DESCRIPTION	7
2.1 Firepond 1.2-m Telescope System	8
2.2 The Optical Tracker Package	9
2.3 The Fast Steering Mirror	12
2.4 Quad Tracker Electronics	13
2.5 Track-Data-Acquisition System	15
2.6 Stellar Scintillometer	17
3. SYSTEM PERFORMANCE	19
3.1 Tracker Noise Sources	19
3.2 Ultimate Bandwidth and Noise Floor Tests	20
3.3 Star Tracking Bandwidth Capabilities	23
3.4 Calibration of the Optical Error Signals	25
3.5 Angle-of-Arrival Calibration	25
3.6 Tracker Scale-factor Balance	26
4. TILT ANISOPLANATISM RESULTS	29
4.1 Description of an Observing Session	29
4.2 Double-Star Selection	30
4.3 Summary of Data Runs	31
4.4 Typical Processing of Results	33
4.4.1 Rotation of Data	34
4.4.2 Differential Tilt Power Spectral Densities	35
4.4.3 Determination of System Noise	37
4.4.4 Normal vs Flipped Differential Tilt	37

4.5	Monitoring of Atmospheric Variables	37
4.6	Tilt Anisoplanatism Data	42
4.6.1	Tilt Anisoplanatism vs Atmospheric Coherence Length	42
4.6.2	Tilt Anisoplanatism vs Isoplanatic Angle	43
4.7	Comparison of Firepond Data with Theory	47
4.7.1	Tilt Anisoplanatism vs Double-Star Separation	47
4.7.2	Tilt Anisoplanatism vs Normalized Separation	47
4.7.3	Longitudinal vs Lateral Component Magnitude	49
4.8	Power Spectral Density of the Differential Tilt	49
5.	CONCLUSIONS	57
	ACKNOWLEDGMENTS	59
	REFERENCES	61

## LIST OF ILLUSTRATIONS

Figure No.		Page
1-1	Differential Tilt Measured on Double Stars as a Function of Normalized Star Separation with Calculations Using Several Atmospheric Models	4
1-2	Tilt Anisoplanatism as a Function of Path Length Normalized to Atmospheric Coherence Length and Isooplanatic Angle	4
2-1	Tilt Anisoplanatism Measurement Equipment	7
2-2	Firepond 1.2-m-Aperture Telescope with the 60-cm-Aperture Finder Telescope	8
2-3	Firepond 1.2-m-Aperture Telescope with the Binary Star Tracking Equipment Mounted on the Azimuth Axis	9
2-4	Optical Schematic of Binary Star Tracker	10
2-5	Quad Detector with Four Photomultiplier Tubes	11
2-6	Quad Detector Pyramid and Circular Stop	12
2-7	Construction of the Fast Steering Mirror	13
2-8	Quad Tracker Electronics	14
2-9	Data-Acquisition System	16
2-10	Twinkle Meter Schematic	18
3-1	Test Setup for Quad Trackers	20
3-2	Power Spectral Density of Fast Steering Mirror Position During High-Optical-Turbulence Tracking Tests	21
3-3	Power Spectral Density of Fast Steering Mirror Position During Optical Tests with Extremely Low-Turbulence Level	22
3-4	Closed-Loop Response of Fast Steering Mirror in Caged Mode	23
3-5	Tilt Power Spectral Density on a 2nd-Stellar-Magnitude Star	24
3-6	Tilt Power Spectral Density on a 4.5th-Stellar-Magnitude Star	24
3-7	Tracker Balance While Tracking $\gamma$ Del	27
4-1	Some Double Stars Visible from the Firepond Site at Various Times of the Year	30

Figure No.		Page
4-2	Analog Chart Record of Differential Tilt Measured on $\gamma$ Del (48.5- $\mu$ rad Separation)	33
4-3	Determination of Separation Direction of Double-Star $\gamma$ Del	35
4-4	Samples of Tilt Power Spectral Densities Measured on $\zeta$ UMa (Mizar)	36
4-5	Determination of Differential Tilt System Noise on $\zeta$ UMa (Mizar)	38
4-6	Comparison of Differential Tilt Measurements Under Normal and Flipped Conditions	39
4-7	Turbulence Profiles Used for Numerical Calculations	40
4-8	Atmospheric Coherence Length $r_0$ Implied from $\alpha$ UMi (Polaris) Tilt During Five Summer Nights	41
4-9	Isoplanatic Angle $\theta_0$ at the Firepond Site During Five Summer Nights	43
4-10	Differential Tilt as a Function of Atmospheric Coherence Length	44
4-11	Tilt Anisoplanatism as a Function of Isoplanatic Angle	45
4-12	Tilt Anisoplanatism as a Function of Path Separation Compared with Calculations Based on Several Atmospheric Models	46
4-13	Tilt Anisoplanatism as a Function of Path Separation Normalized to Atmospheric Coherence Length and Isoplanatic Angle	48
4-14	Ratio of Longitudinal and Lateral Components of Tilt Anisoplanatism for Firepond Data	50
4-15	Location of Albany, Portland, and Chatham Weather Stations with Respect to Firepond	51
4-16	Wind Profiles at Albany, Portland, and Chatham During the Evening of 10 June 1986	52
4-17	Power Spectral Density of Total Differential Tilt of $\zeta$ UMa on the Evening of 10 June 1986 Compared with Theoretical Calculations	53
4-18	Typical Power Spectral Densities Taken During the Evening of 10 June 1986 on the Double-Star $\zeta$ UMa (Mizar)	55
4-19	Power Spectral Density for Three Double-Star Separations for Longitudinal and Lateral Components During the Evening of 10 June 1986	56

## LIST OF TABLES

<b>Table No.</b>		<b>Page</b>
3-1	Tracker Noise Characterization Using Test Source	19
4-1	Summary of Measurements of Double Stars	32
4-2	Atmospheric Parameters for Five Turbulence Models	40

# MEASUREMENTS OF TILT ANISOPLANATISM AT THE FIREPOND FACILITY

## 1. INTRODUCTION AND SUMMARY

The turbulence-induced wavefront aberrations seen by a telescope can differ significantly over two propagation paths with only slightly different propagation directions. This is of particular concern in adaptive optics systems where the beacon which is used to measure the atmosphere-induced aberrations is not viewed in exactly the same direction that compensation is to be performed. Fried<sup>1</sup> has shown that significant degradation in antenna gain is experienced in adaptive optics systems if the separation between the sensed path and the corrected path is large as compared with the isoplanatic angle, the angle over which the atmosphere introduces a constant phase change. The differences in atmospheric aberrations over these paths is known as the phenomenon of anisoplanatism.

In this report, we deal with the lowest order of anisoplanatism, that is, the differential tilt induced by the atmospheric turbulence between two objects separated by a small angle. We call this tilt anisoplanatism. The tilt anisoplanatism is a random phenomenon. For small path separations its magnitude increases with path separation and it is independent of wavelength. While larger-aperture systems provide some aperture averaging for tilt anisoplanatism, it is most bothersome in large-aperture short-wavelength systems whose diffraction-limited beam width is small. For instance, tilt anisoplanatism limits the field-of-view of a high-resolution astronomical guiding system where a bright star is tracked to stabilize the telescope close to the dim star which is being observed. When working with satellites, laser radars and communications systems are affected by tilt anisoplanatism because the transmitted beam has to be pointed ahead of the received tracker beam in order for the transmitted beam to intercept the satellite.

Lincoln Laboratory has investigated tilt anisoplanatism by observing binary stars (two stars separated by a very small angle) with the 1.2-m-diam. Firepond telescope and measuring the differential tilt introduced by the atmosphere. Precision tracking equipment was constructed to track each of the double stars of a pair. The differential tilt was obtained directly from the difference of the tracked star positions. The results unfortunately show a factor-of-3 higher magnitude of tilt anisoplanatic error than previously believed.

### 1.1 HISTORICAL BACKGROUND

For over a half-century, astronomers have known of the harmful effects of what is now called tilt anisoplanatism. This effect manifests itself when observing weaker star fields while the telescope's line-of-sight is stabilized on a brighter guide star. As the radial distance from the guide star increases, there is a gradual decorrelation of the instantaneous position of the star image. Serious limitations are thus imposed on the usefulness of a high-bandwidth guiding system

to steady all the stars within a wide field-of-view. On the other hand, improvement in the overall resolution of up to a factor-of-2 can result within a small field during planetary and double-star work. Beyond this so-called isoplanatic patch size, the effectiveness of tilt removal falls away and discernible differential motion is present even at the edge of a planetary disk. This can be easily seen by experienced planetary observers as rapid disk distortions and apparent displacement ripples of separate lunar crater images.

Dr. Frank Schlesinger,<sup>2</sup> an early investigator in seeing effects, noticed in 1927 that photographic images of trailed stars showed almost parallel motions. This region of high position correlation was referred to as a "parallax field." The small differential displacements observed in his measurements were dismissed as measurement errors! In 1956, while developing a fast "seeing compensator," J.H. DeWitt, R.H. Hardie, and C.K. Seyfert<sup>3</sup> proposed using their new device to measure the "coherence of seeing." They proposed to steady the image of Jupiter and observe the position fluctuations of its satellites at various angular separations from the planet. Unfortunately, the results of this proposed measurement could not be found. In any event, the differential motions they were to measure are quite apparent when visually observing the planet Jupiter and its moons.

The magnitude of differential tilt is closely related to the turbulence strength at high altitudes where the paths to the two stars do not overlap. In the early 1960s, A.H. Mikesell of the US Naval Observatory set out to measure high-altitude turbulence strength. Mikesell<sup>4</sup> used a portable high-bandwidth scintillometer which could be easily aimed at stars from an aircraft. His measurements demonstrated that, even at 37,000 ft, one-fourth of the twinkle amplitude remains. This has been confirmed by the fact that balloon flights instrumented for the purpose of high-resolution photography of the sun required altitudes of 80,000 ft and more to get above harmful seeing disturbances.

Given these findings it was not surprising that, in our early experiments, we observed strong effects of tilt anisoplanatism for binary stars of only 108- $\mu$ rad separation. While none of the early astronomical observations addressed quantitatively the magnitude of these effects, we attempted to measure directly the magnitude of the differential tilt. These initial measurements at the Firepond Facility in Westford, Massachusetts used two existing TV trackers and showed a sizable tilt anisoplanatism, which was much higher than would be predicted by commonly used atmospheric models. The accuracy of these measurements was poor and the measurement bandwidth was limited by the TV frame rate to  $\sim 15$  Hz, so we decided to build suitable tracking equipment and to repeat the measurements with greater precision. This report describes this experimental system and the results of the measurements.

## 1.2 EXPERIMENTAL EQUIPMENT

Two quad trackers were built for measuring tilt anisoplanatism. Each tracker used an optical pyramid to divide the image into four quadrants, whose intensities were measured with photomultipliers and combined to generate the beam-position error signals. The error signals were used to drive a fast steering mirror in front of the optical pyramid to center the star image on the

detector system. The sum of the fast steering mirror position and the residual tracker error signal was used as the estimate of the tilt seen by the tracker. Two similar trackers were constructed to look through the same telescope, so that the pointing jitter of the telescope would cancel in the subtraction process to obtain the differential tilt. The remainder of the optical system was constructed to minimize uncommon jitter, for instance, by paying attention to thermal turbulence around the optics and stability of the mounts.

The equipment was constructed, functionally checked out, and the first double-star differential tilt measurements were made in the summer of 1985. While these data were of much higher quality than the initial TV measurements, the sensitivity of the system fell short of what was expected. Several improvements were made to the tracking system, including modifying the optical setup and reducing the levels of various noise sources. In parallel with these modifications, a scintillometer was designed and constructed so that the isoplanatic angle could be measured during data taking. These improvements were incorporated into the experimental system in early 1986, and the system was ready to collect tilt anisoplanatism data on double stars in the summer of 1986.

Measurement of tilt anisoplanatism requires the measurement of very small differential tilt from two stars, and consequently requires sophisticated tilt tracking equipment. Because of this, a considerable portion of this report describes the hardware that was designed and built for this purpose. Sections 2 and 3 describe the design details and performance of the experimental equipment. A reader not interested in the details of equipment can proceed directly to Section 4 where the experimental results are presented. A brief review of the most-significant findings is given below.

### 1.3 SUMMARY OF RESULTS

Figure 1-1 shows two-axis differential tilt measured on three binary pairs with separations ranging from 48 to 108  $\mu\text{rad}$ . The zenith normalized differential tilt is plotted against the normalized star separation. On the same figure are plotted values of tilt anisoplanatism, calculated by the Optical Sciences Company, using various atmospheric models. We note that all the measured data are higher than the SLC day model predictions but are bounded on the high side by the HV-50 model calculations, except for a few data points. (The SLC and HV models are described later in this report.) Note also that the tilt anisoplanatism magnitude is a large fraction of a microradian for 50- $\mu\text{rad}$  star separation, which is the maximum lead-ahead angle for low-altitude satellites. This is much larger than the usually quoted value of 0.3  $\mu\text{rad}$  as calculated by use of the SLC models. Since the estimated measurement error is less than 0.2  $\mu\text{rad}$ , it cannot account for the large difference.

The two-axis differential tilt shown in Figure 1-1 is made up of unequal components along and transverse to the star separation direction. Theory predicts that the longitudinal component is the square root of 3 times greater than the lateral component for weak turbulence strength. Our measurements consistently showed a ratio of approximately 1.2, which would be the trend for very strong turbulence levels.

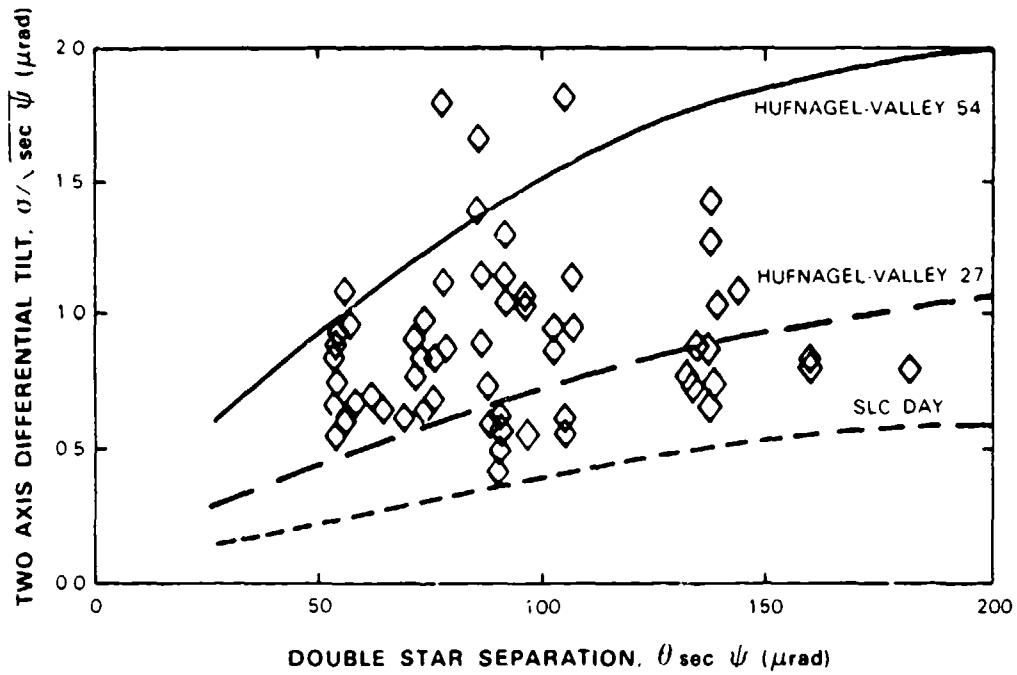


Figure 1-1. Differential tilt measured on double stars as a function of normalized star separation with calculations using several atmospheric models.

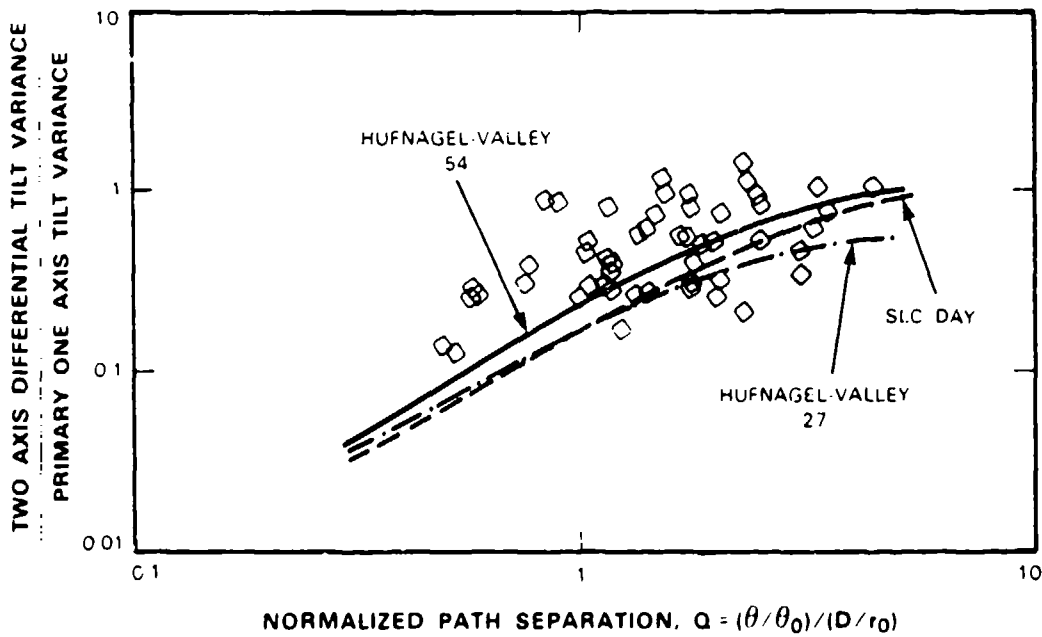


Figure 1-2. Tilt anisoplanatism as a function of path length normalized to atmospheric coherence length and isoplanatic angle.

98694-8

98694-7

During an experimental run, we also measured the isoplanatic angle and atmospheric coherence length on Polaris by observing its scintillation and angle-of-arrival jitter. Figure 1-2 shows the tilt anisoplanatism normalized by the tilt variance to a single star of the pair plotted as a function of star separation normalized by the isoplanatic angle  $\theta_0$ , the atmospheric coherence length  $r_0$ , and the telescope aperture diameter  $D$ . Note that when the theoretical predictions are plotted in this normalized fashion, the curves for all models fall roughly on top of each other. Here, the measured data correlate much better with the predictions based on the various models. While the tilt anisoplanatism values were much higher than predicted, the measured  $\theta_0$  and  $r_0$  corresponded to a stronger turbulence than modeled. Thus, we must conclude that the turbulence strength in the vicinity of the Firepond site is much stronger than predicted by the SLC model.

The power spectral density of tilt anisoplanatism is dependent on the high-altitude wind velocity. Our measurements showed that the shape of the power spectral density could change from minute to minute. However, the measurements also show that most of the tilt anisoplanatism energy occurs at frequencies less than 30 Hz and the energy above 100 Hz is almost negligible.

## 2. EQUIPMENT DESCRIPTION

The overall block diagram of the tracking system is shown in Figure 2-1. The system consists of the Firepond mount for following the double-star motion, two trackers (each having a quad detector and a fast steering mirror), and recording and associated data-gathering equipment. While the Firepond telescope is pointed in the general direction of the double star, each of the trackers is locked-on to a separate star. The optical bias blocks (prisms) are in the system to shift the line-of-sight of each tracker to either of the stars. Since the quadrant detectors have a transfer characteristic which is dependent on the image size (which, in turn, depends on the atmospheric seeing that changes from minute to minute), the system has a fast steering mirror in front of each tracker which was used in a closed loop to track the angle-of-arrival to minimize the quad detector output. By adding the small residual error indicated by the quad detector output to the fast steering mirror position, the quad detector calibration uncertainty due to spot size is minimized. The output of the quad trackers and the fast steering mirror positions are recorded on the computer tape at a 4-kHz rate and processed for various statistics post-mission.

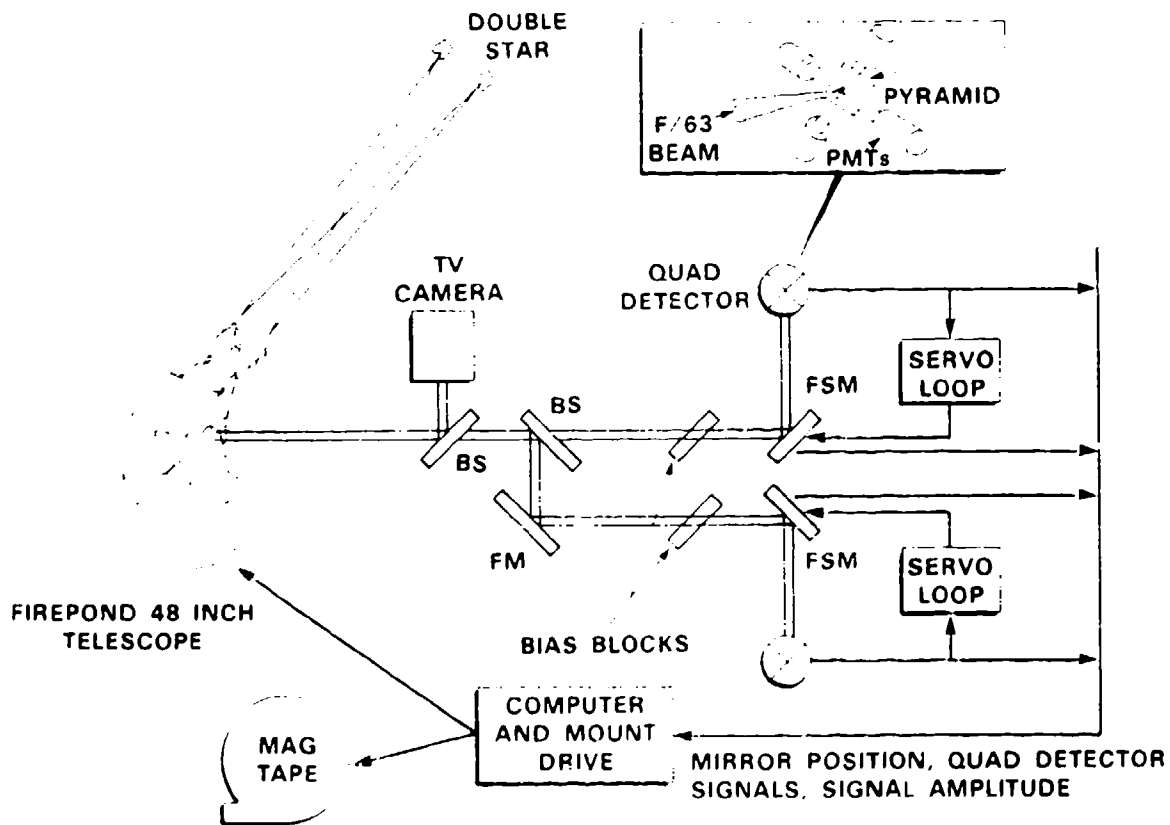


Figure 2-1. Tilt anisoplanatism measurement equipment. (BS = beam splitter, FSM = fast steering mirror, FM = fold mirror, PMT = photomultiplier tube).

## 2.1 FIREPOND 1.2-m TELESCOPE SYSTEM

The Firepond telescope, shown in Figure 2-2, has a 120-cm aperture and a 13.8-cm secondary mirror. The secondary mirror can be tilted in two axes for faster angle tracking to compensate for mount dynamic lag and for jitter. The secondary mirror can also be adjusted with a servo to focus at different ranges. The mount angular velocity and acceleration capabilities are greater than  $10^\circ/\text{s}$  and  $10^\circ/\text{s}^2$ , which is adequate for tracking low earth-orbit satellites. The Firepond telescope is described in Reference 5.

One of the main attributes of the mount is its extremely smooth control system. Both azimuth and elevation axes are supported by ball bearings and are driven by direct gearless dc torque motors. The mount position, reported by 24-bit optical angle encoders, is subtracted from the mount commands in the control computer and the difference, after compensation, is used to drive the mount. The amplification of drive signals is accomplished by controlling the field current of dc generators driven with a 60-Hz motor. While there are several servo modes, normally the system is used in Type II software compensation mode. In this mode, the closed-loop servo bandwidth is  $\sim 2$  Hz in azimuth and  $\sim 1$  Hz in elevation. The secondary mirror tip, tilt servos, whose closed-loop bandwidth is  $\sim 25$  Hz, can be used to widen the pointing bandwidth in several cascade pointing modes. The secondary mirror is supported by a flexure pivot and tipped and tilted with dc motor-driven lead screws. Secondary position is reported by LVDTs (Linear Variable Differential Transformers) with a resolution of  $\pm 0.375 \mu\text{rad}$ .

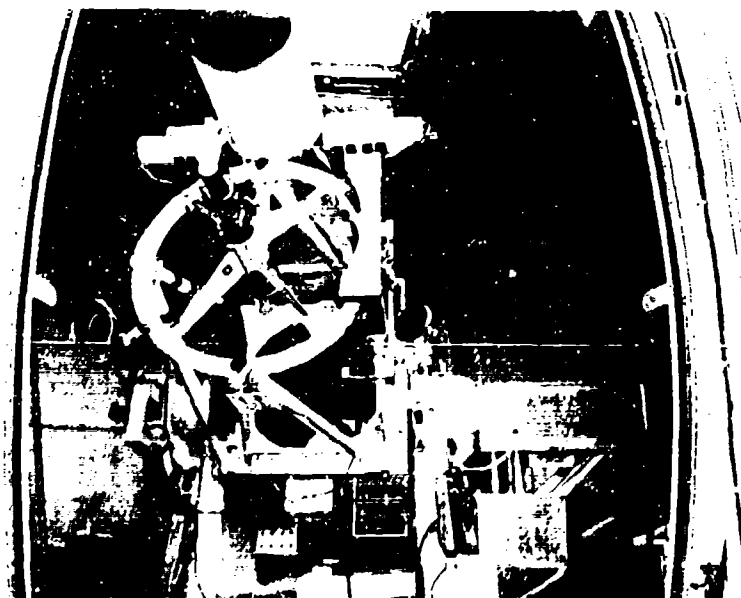


Figure 2-2. Firepond 1.2-m-aperture telescope with the 60-cm-aperture finder telescope.

104376-1

The telescope is controlled by two Gould SEL 32 27 computers. Various modes of pointing are available under software control. During the tilt anisoplanatism measurements, a FK-4 star catalogue containing ~1600 stars was used to point the telescope toward a desired double star, and small-angle biases were added through handwheels to position the star in the field-of-view at the desired spot.

A 60-cm Newtonian finder telescope is mounted on top of the Firepond 120-cm telescope. An 11-cm-diam. patch of this telescope aperture was used for the scintillometer (described later) which we used to measure the isoplanatic angle during the double-star tracking experiments.

The telescope is housed in a dome which is slaved to the telescope azimuth. The dome provides good protection against disturbances and biases caused by wind and sun loading on the telescope.

## 2.2 THE OPTICAL TRACKER PACKAGE

The double-star tracker consists of two identical null tracking systems rigidly mounted on the telescope and rotated in azimuth as shown in Figure 2-3. The optical layout is shown in Figure 2-4.



*Figure 2-3. Firepond 1.2-m-aperture telescope with the binary star tracking equipment mounted on the azimuth axis.*

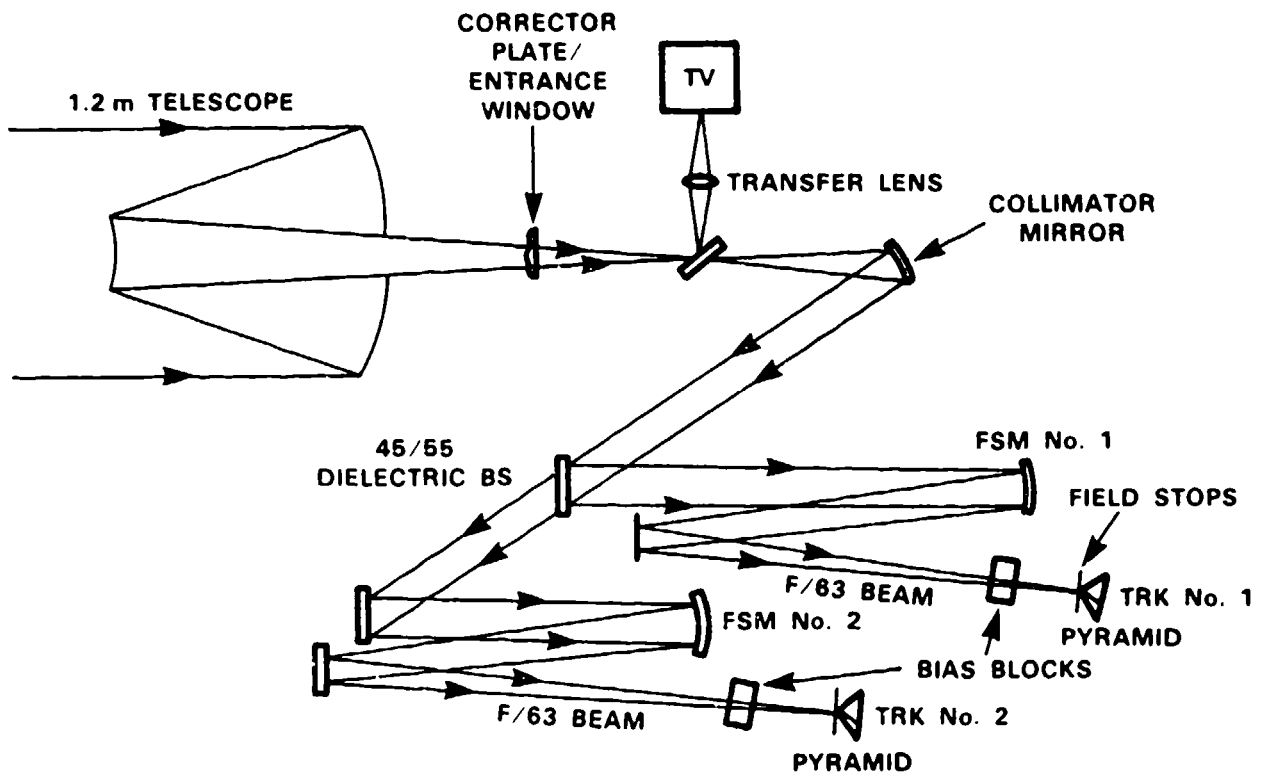


Figure 2-4. Optical schematic of binary star tracker.

For this experiment, the Firepond telescope was configured as an  $f/32$  Cassegrain, which is a departure from the normally used  $f/200$  Cassegrainian configuration, with a consequent increase in spherical aberration introduced by the system. This aberration was corrected with a small fused silica corrector plate located 47 in before the focus. The corrector was null figured *in situ* using Polaris as the test source. The corrector also served as the input window to the thermally insulated optics package.

The first component in the optical package is a thin-film beam splitter (a pellicle) that reflects 2.5 percent of the light through a transfer lens into a sensitive intensified silicon intensifier target (ISIT) camera which is used to guide the star image into the field-of-view of the trackers. This TV also provides the position angle of the binary pair in the tracker coordinates, so we may identify the longitudinal and lateral measurement axis for data-reduction purposes. The transmitted divergent beam is collimated by a spherical mirror that also re-images the 1.2-m entrance pupil into the exit pupil plane well beyond the next element. The astigmatism introduced by the spherical mirror is corrected with a special mounting cell for the spherical mirror which introduces astigmatism of the opposite sign with sufficient precision that diffraction-limited performance was easily achieved.

92839-10

The next element is the 45/55 beam splitter. From this point in the path, the collimated beams proceed to each tracker. Great effort was expended to ensure that the trackers were optically identical and to ensure that each would have identical image and magnification characteristics.

The next element in each path is the spherical fast steering mirror with a focal length of 92 in. This focal length was chosen to provide a blur circle large compared with the pyramid tip blunting errors, as well as having sufficient depth of focus at the field stop which must be positioned slightly ahead of the prism tip. The convergent beam next passes through the bias blocks which provide a means of fine steering or offsetting the final lateral position of the focal spot. This is necessary for selecting either the primary or companion of the binary star. The bias blocks are mounted in a roll (position angle) and tilt (separation) servo-driven cage controlled by the console operator. Typically, both bias blocks were tilted to share the displacement value maintaining the best focus. Tilting the blocks introduces only trivial aberrations, 100 times smaller than the typical seeing disk.

The quad error sensors are shown in Figure 2-5. A highly reflective pyramid, shown in Figure 2-6, divides the focal spot into four beam segments which are directed to four EMI Model 9826 photomultiplier tubes. The photomultiplier tubes have a bialkali photocathode which has its peak quantum efficiency at  $\sim 0.35\text{-}\mu\text{m}$  wavelength. The faces of the photomultiplier tubes are tilted at slight angles to prevent reflections into opposite tubes. A circular stop is mounted in front of the pyramid to admit only one star into each quad sensor. This aperture is drilled to subtend  $37\ \mu\text{rad}$ , which is small enough to separate star pairs but large enough to admit the full seeing blur.

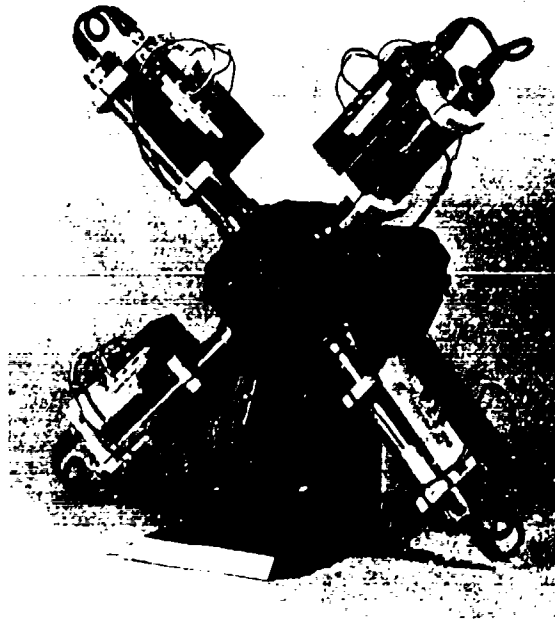


Figure 2-5. Quad detector with four photomultiplier tubes.

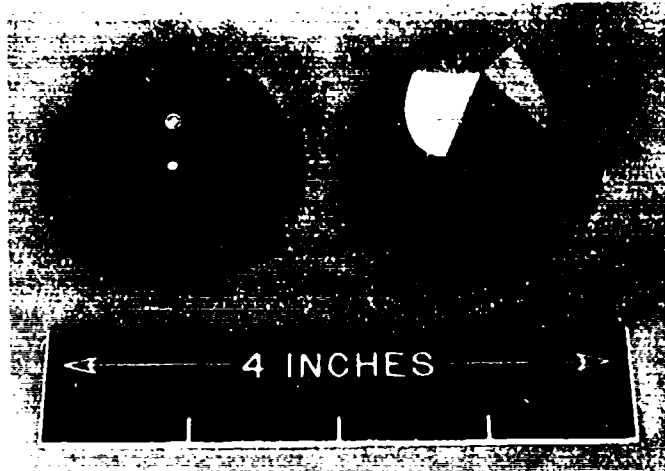


Figure 2-6. Quad detector pyramid and circular stop.

104376-4

### 2.3 THE FAST STEERING MIRROR

The fast steering element is a 5-cm-diam. mirror, mounted on a ring which is supported by three flexures and driven by three piezoelectric actuators. Four linear variable differential transformer (LVDT) sensors are spaced at  $90^\circ$  intervals along the ring to provide elevation and azimuth readings of the mirror position. We chose the lead-zirconium titanate (PZT) actuator-driven fast steering mirror for keeping the target image on boresight, as it most clearly guaranteed a performance level margin for the experimental program. PZT actuators are capable of high-frequency response; our mirror and driver can typically achieve a frequency response of 500 Hz in closed-loop mode.

Construction details of the mirror are shown in Figure 2-7. The mirror is driven by three PZT units spaced  $120^\circ$  apart. This arrangement prevents mechanical overconstraint. The 3-axis motion is resolved into two mutually perpendicular axes electronically.

Four LVDT core pieces, one for each transformer, are bolted to four symmetrically displaced extension tabs on the mirror edge. These tabs are in the plane of the mirror surface. The coil portion of the LVDTs is mounted to the fixed-mirror support stand and is adjustable along the measuring axis, thus providing a means of nulling the output voltage at the zero tilt position.

The 5-cm-diam. mirror is machined from a solid aluminum billet, stress relieved, and nickel plated before optical surfacing and high-reflectivity coating. Since final focusing is accomplished with these mirrors, they are finished with a shallow concave spherical surface of 184-in radius.

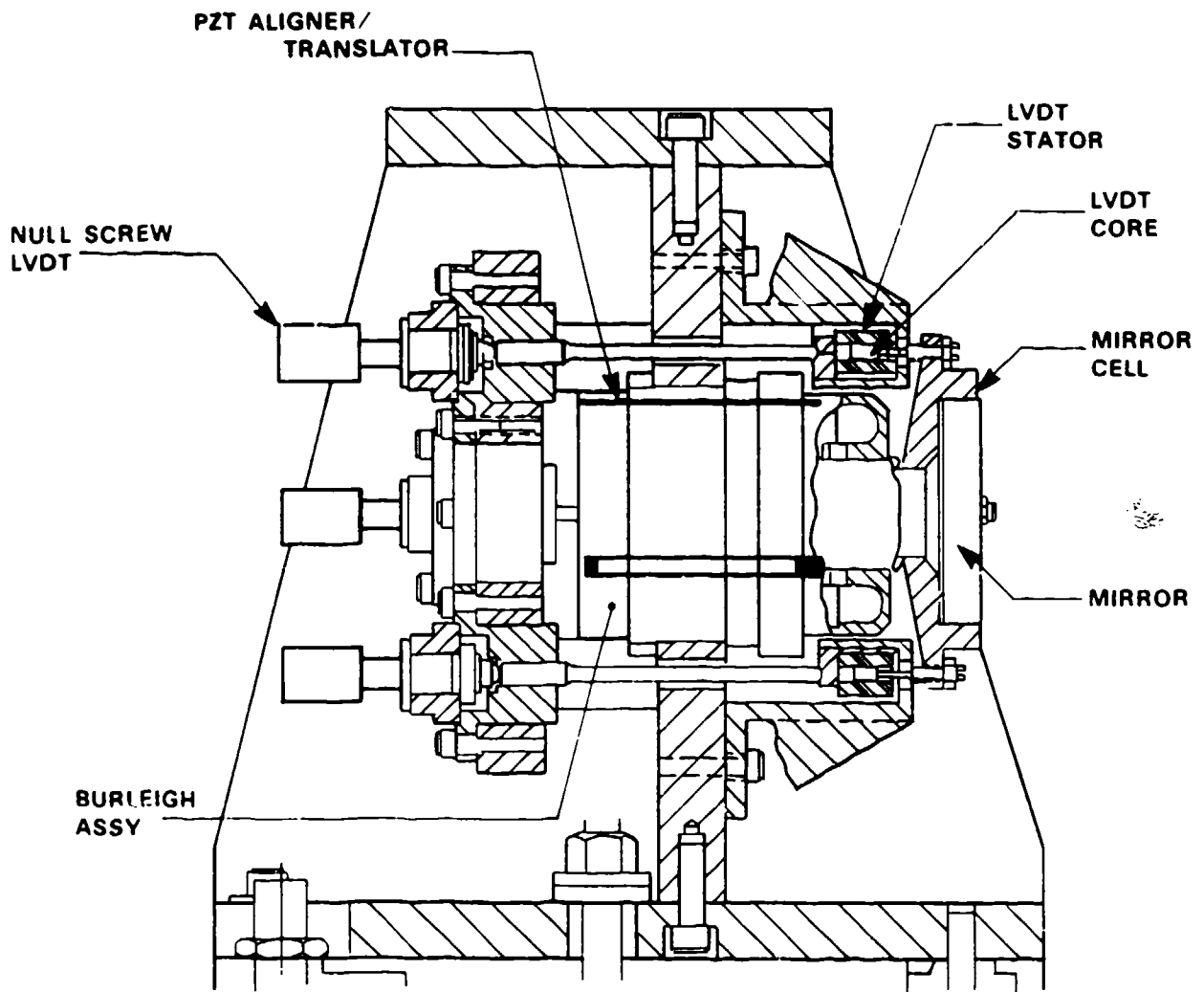


Figure 2-7. Construction of the fast steering mirror.

## 2.4 QUAD TRACKER ELECTRONICS

Two identical trackers consisting of a quad sensor, fast steering mirror, and servo system were built for the tilt anisoplanatism measurements. As shown by the electronics block diagram of Figure 2-8, the servos can be operated in two modes: caged and tracking.

In the caged mode, the servo loop holds the mirror stationary at its zero position for testing and alignment purposes. The servo is caged by feeding back the mirror position using the LVDTs. A 10-kHz oscillator, after leveling and amplification, provides a 3-V rms drive for the LVDTs. Single-axis output values are derived from the sum and difference of two orthogonal LVDT sensors. This technique compensates tilt measuring errors incurred by residual mirror

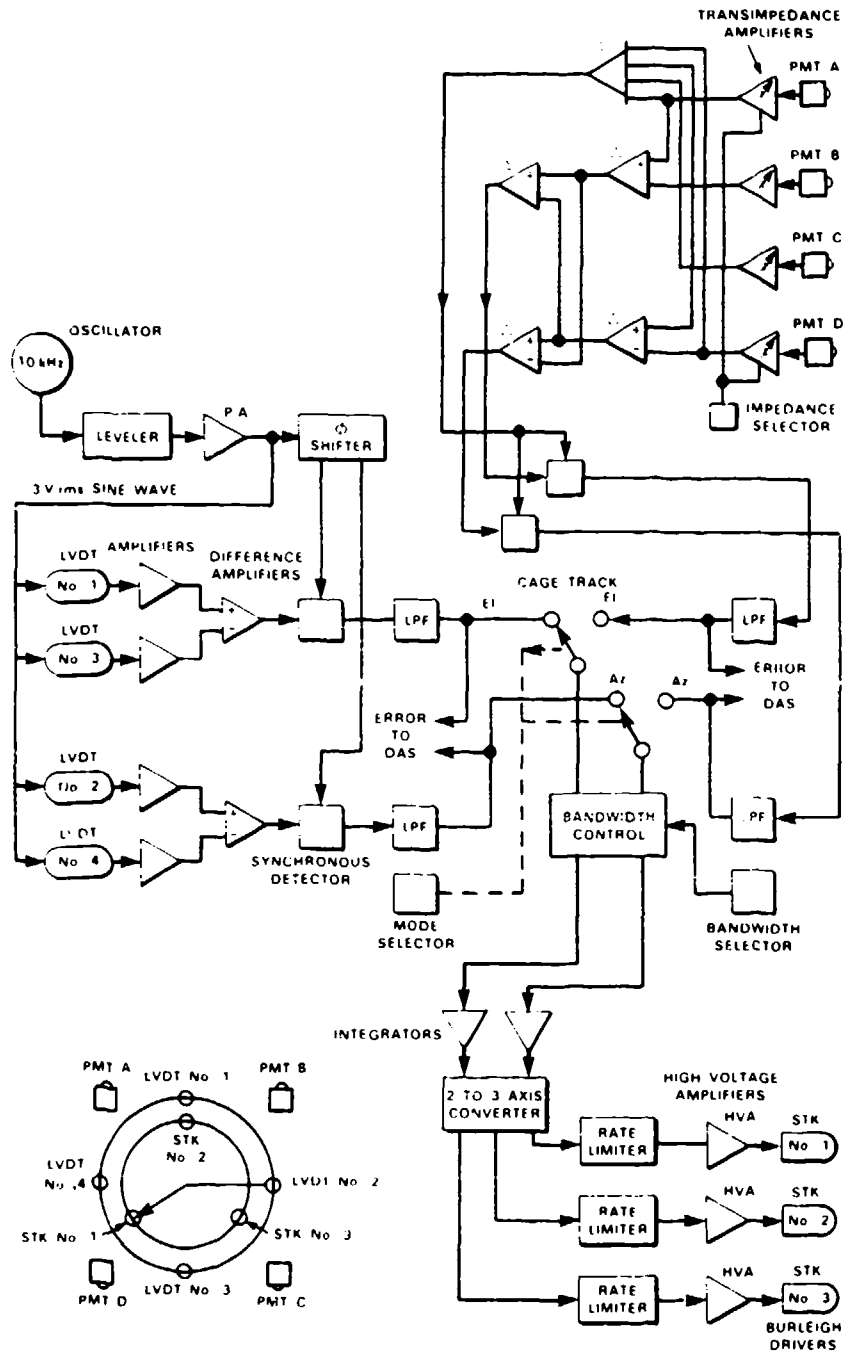


Figure 2-8. Quad tracker electronics. (DAS = Data-Acquisition System, LPF = low-pass filter, LVDT = linear variable differential transformer, PMT = photomultiplier tube).

92839-12

translation. Synchronous detection of the LVDT outputs allows the magnitude and the direction of the mirror position to be determined. After filtering and amplification, the detector outputs provide a voltage proportional to mirror motion with 16.5-mV,  $\mu\text{rad}$  angular responsivity. These position signals are fed into the servo system compensation circuits to keep the mirror position at the nominal zero position. Since the LVDTs produce an azimuth and elevation mirror position signal, but the mirror drive is accomplished by three PZT stacks, a 2- to 3-axis converter circuit is used before the rate limiters and high-voltage stack drivers.

In the tracking mode of operation, the error signals are obtained from the quad sensors. The photomultiplier tube output currents are converted to voltages by transimpedance amplifiers. Three values of load resistance can be selected to compensate for the variation in stellar brightness. Azimuth and elevation position error signals are obtained by combining sum and difference signals as shown in Figure 2-8. By normalizing the differences with respect to the sum, position errors independent of the stellar brightness are obtained.

In either the caged or the tracking mode, the servo tries to null the error. Varying the gain of the amplifiers preceding the integrators in the Type I loop adjusts the bandwidth of the servo response. The linear control of the servo can provide a maximum safe voltage of 1000 V to the actuators, which corresponds to  $\pm 118 \mu\text{rad}$  from the mirror center position or  $\pm 10 \mu\text{rad}$  in the sky coordinates.

## 2.5 TRACK-DATA-ACQUISITION SYSTEM

The Firepond control computer collects system status data and records them on magnetic tape for post-mission data analysis. Numerous data items are sampled at various data rates and organized into tenth-second-interval data blocks for recording. The double-star experiment utilizes this feature for data collection. Since the normal Firepond real-time sampling rates are not high enough, a new data-acquisition system was built to collect the tracking data at a 4-kHz sampling rate. This system samples the mirror positions, quad detector outputs, and star signal amplitude for both trackers.

Figure 2-9 shows the block diagram of the new Data-Acquisition System. The ten channels of data inputs are smoothed with 5-pole Butterworth low-pass filters with a -3-dB cutoff at 1 kHz to suppress aliasing. Then, all ten channels are sampled and held simultaneously at a 4-kHz rate. Between samplings, an analog multiplexer delivers the data to the 12-bit analog-to-digital converter which feeds its outputs into a FIFO (first-in first-out) memory. The contents of the FIFO memory are transmitted to the computer in a direct-memory-access mode via a multi-purpose interface card capable of a throughput of 1 Mbyte/s. The 4000-S/s per channel sampling rate is well within this capacity. These data are buffered into tenth-second data blocks and recorded on magnetic tape along with other Firepond system parameters. The start and end of the digitization and data recording are controlled by the operator.

Various data processing and analysis programs are available for analyzing the Firepond recorded data. These programs were utilized in the double-star data analysis as well. Several new

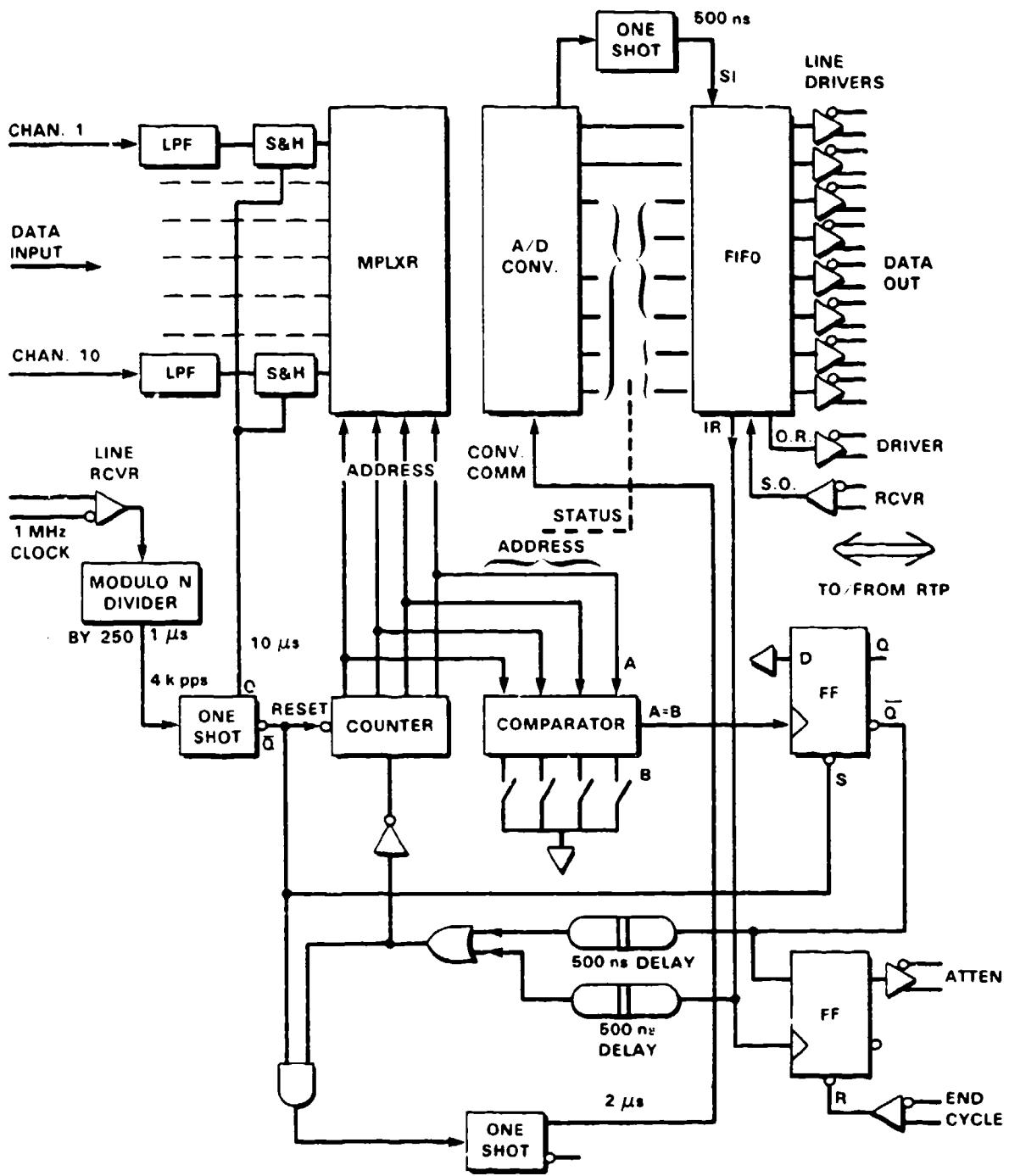


Figure 2-9 Data-Acquisition System. (LPF = low-pass filter, S&H = sample and hold, FIFO = first-in;first-out memory).

92839-13

processing programs were required for the processing and analysis of the differential tilt data. The experiment-related software operated in two phases: In the first phase, various statistics and parameters were computed for individual data-collection runs. The second phase entered these data into a double-star data base where additional conversions took place in order to present the data and statistics in a convenient form. The results section gives a reasonable sample of the results which were obtained by the use of these software.

## 2.6 STELLAR SCINTILLOMETER

During checkout runs, we observed that on nights when star twinkle was strong, the differential tilt was also large. These observations quickly led to the design and construction of what we affectionately call the "twinkle meter." The twinkle meter simply measures the star light scintillation with an 11-cm-diam. aperture. Loos and Hogge,<sup>6</sup> have shown that an 11-cm-aperture scintillometer weights the atmospheric structure function ( $C_n^2$ ) with altitude in approximately the same manner as the isoplanatic angle. Thus, the scintillation amplitude can be measured and converted directly to isoplanatic angle, as described in Section 4.5. The twinkle meter shared a portion of the 60-cm Newtonian Finder, which rides atop the main telescope. The field-of-view of the scintillometer was limited to 100  $\mu$ rad to view only one star.

The block diagram of Figure 2-10 shows how the instrument works. Light falling on the photomultiplier is converted to an electrical signal which is amplified and separated into its dc and ac components. The true rms-to-dc converter provides a voltage proportional to the ac fluctuations of the stellar brightness. The dc component is proportional to the brightness. The ratio of the two components is scaled so that 10 V corresponds to 100-percent modulation.

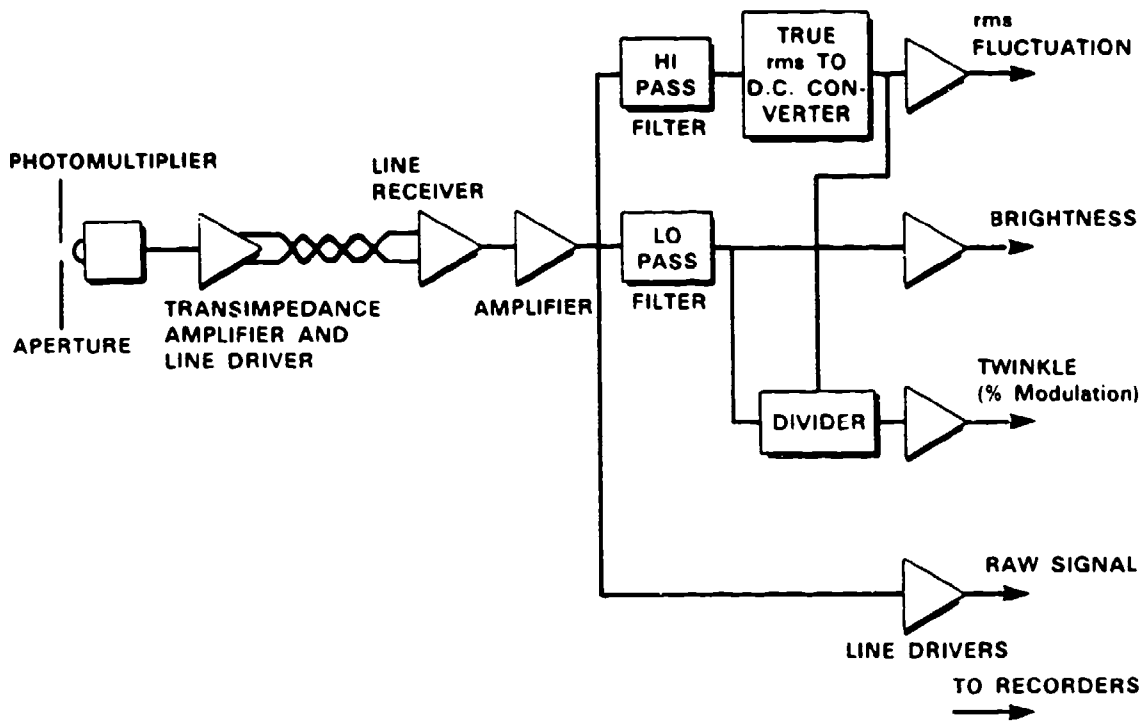


Figure 2-10. Twinkle meter schematic.

92839-14

### 3. SYSTEM PERFORMANCE

Because the expected values of tilt anisoplanatism are small, its measurement requires a precise and well characterized instrument. The important characteristics which determine the accuracy of the measurements are system sensitivity, bandwidth, and angle calibration. This section summarizes the test results of a few of the many tests that were performed. The techniques of system calibration before data-taking sessions are also described.

#### 3.1 TRACKER NOISE SOURCES

A total system noise of 130 nrad (referenced to the sky space) was directly measured for a 4th-stellar-magnitude equivalent light source. Table 3-1 shows the measured or estimated magnitude of the various sources of noise.

<b>TABLE 3-1</b>		
<b>Tracker Noise Characterization Using Test Source (0.5- to 100-Hz Bandwidth)</b>		
<b>Error Contributor</b>	<b>Method</b>	<b>Noise (nrad rms)</b>
Unshared Path Turbulence	Measured	24
Total System Electronics	Measured	9
Pyramid Blunting	Computed	20
Focus Error	Computed	10
<b>RSS</b>		<b>34</b>

Using a bright point source (about 0th-magnitude equivalent) located at the Cassegrainian focus with the telescope pointed out in an operational condition, we found that unshared path disturbances originating within the optical train contributed 24 nrad. The extra bright source reduced other noise sources, such as photomultiplier tube noise, to a negligible value. A very short and harmless unshared path region could not be measured. This region is just a few centimeters of path before and after focus, where the separate cones of light emerge as separate beams and form the closely spaced images of the double star and then recombine. Because this path is sealed with the corrector plate and insulated with the same care as the entire package, we felt that this region contributed a negligible error.

The electronic noise was measured to be 9 nrad by shorting the input to the transimpedance amplifiers and processing the output noise. The centroid determination errors due to pyramid blunting and defocusing were estimated at 20 nrad.

These measured and estimated noise components are small when compared with total measured system noise of 130 nrad, which implies that the main contributor is the photomultiplier noise. The photomultiplier noise was estimated to be 124 nrad by subtracting the other noise sources from the total measured system noise. We were unable to confirm by calculations that these implied noise levels should be expected, because we did not have the exact gain characteristics of the photomultiplier tubes and precise knowledge of the optical transmission.

These low noise values were never observed while tracking 4th-magnitude stars because star images are typically 10- to 15- $\mu$ rad diameter and beset with scintillation and high-frequency shape disturbances. However, the actual noise level under average seeing conditions is low compared with the typically measured differential tilt. During the experiment, the noise was estimated from control measurements (when both trackers tracked the same star) and was subtracted from the data, as explained later.

### 3.2 ULTIMATE BANDWIDTH AND NOISE-FLOOR TESTS

Both closed- and open-loop performance testing of the tracker and fast steering mirror system was performed at our optics test facility where we set up and tested the fast steering mirrors and electronics as they would be used in the final optics package. Each mirror was, in turn, provided with a collimated input beam and the reflected convergent beam was focused on the quad photomultiplier error sensor as shown in Figure 3-1.

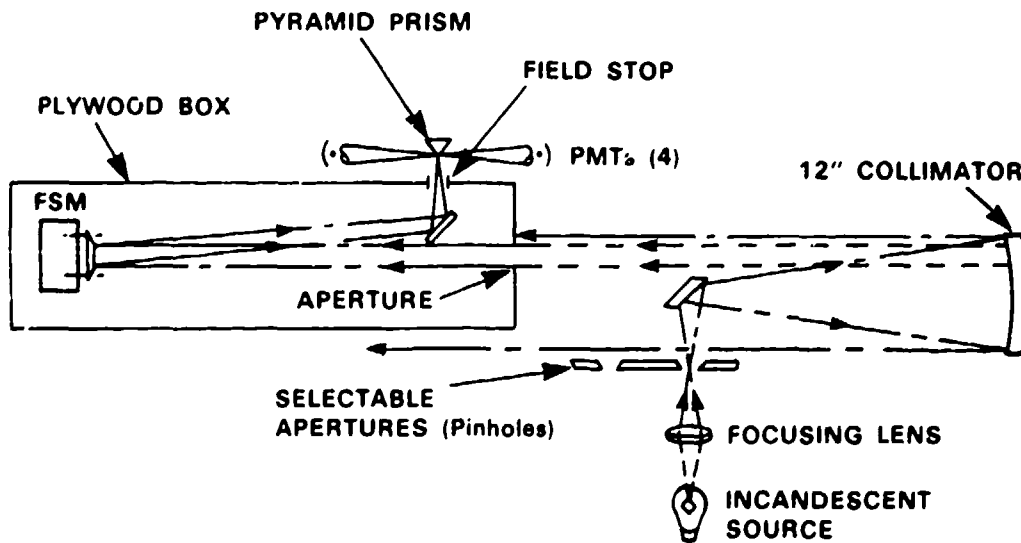


Figure 3-1. Test setup for quad trackers.

In this test setup, the tracker should hold the fast steering mirror stationary, if there is no turbulence in the optical path. But if there is turbulence, we should see line-of-sight motion which is characteristic of atmospheric turbulence. The trackers were used to track a light source whose diameter corresponds to the expected average blur circle for the Firepond telescope, and the mirror motion was analyzed by computing a power spectral density. Figures 3-2 and 3-3 show the closed-loop mirror position power spectral density (PSD) during extremely high and very low turbulence levels. The strong atmospheric turbulence of Figure 3-2 was simulated by introducing a heat gun blast directly along the optical path. Measurement of the PSD for the low-turbulence condition shown in Figure 3-3 required enclosing the optical path to create a nearly stagnant seeing condition. The source brightness was set to a maximum value just below sensor saturation, because these tests were designed to demonstrate the ultimate tracking bandwidth capabilities.

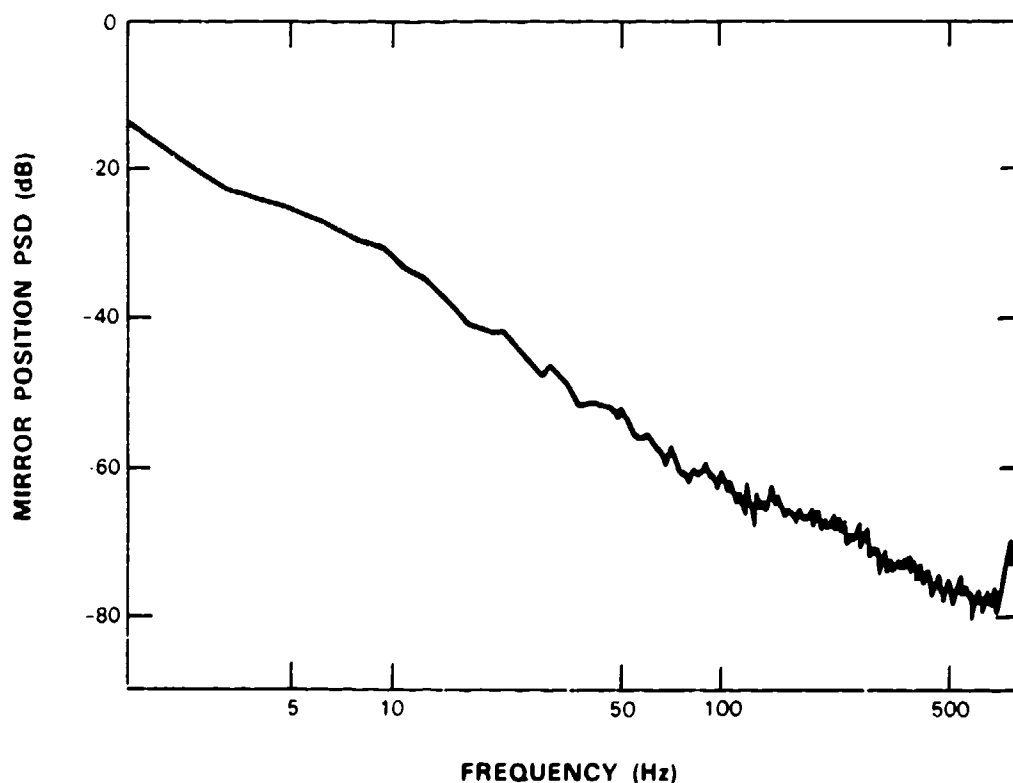
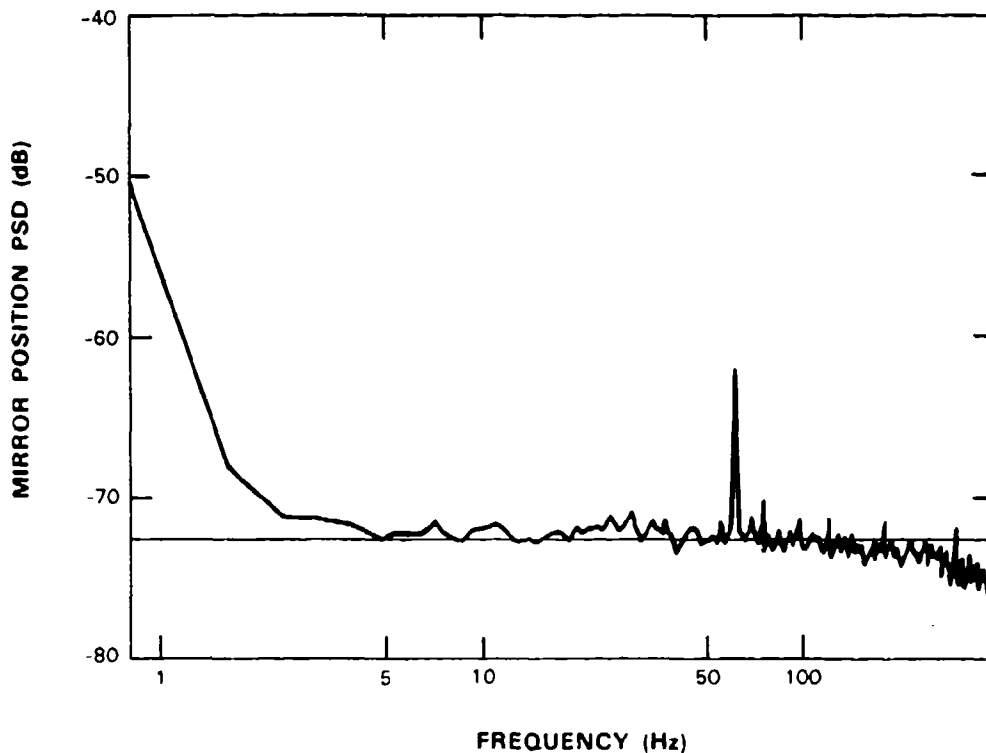


Figure 3-2. Power spectral density of fast steering mirror position during high-optical-turbulence tracking tests. The high-turbulence level produced an  $\sim 29\text{-}\mu\text{rad}$  angle jitter referenced to the 1.2-m Firepond telescope object space.



92839-17

Figure 3-3. Power spectral density of fast steering mirror position during optical tests with extremely low-turbulence level. This low-turbulence simulation produced only  $\sim 20$  nrad of total angle jitter referenced to the 1.2-m Firepond telescope object space.

During these tests, the loop gain of the Type I servo was set as high as possible. We were able to get loop bandwidths as high as 1000 Hz during these high-signal-level conditions. Note from Figure 3-2 that the first serious resonance is just beyond 800 Hz which is typical for each axis on both trackers. The low-turbulence measurement was performed to demonstrate the ultimate closed-loop noise-floor level on a nearly ideal stationary source. Note that the 60-Hz power line interference which is evident at these low values of mirror motion in Figure 3-3 are hidden in the high-turbulence measurement of Figure 3-2.

Caged mode tests were performed to measure the phase shift inherent to this particular tracker. This measurement is important only if the mirrors were to be used in open-loop beam-pointing applications. Since the binary star experiment depends on subtracting one tracker position from the second tracker, phase errors are unimportant so long as they are closely matched for each tracker. It is of some interest that the  $45^\circ$  phase point under open-loop condition occurs at 160 Hz. The measured caged mode mirror response curve is shown in Figure 3-4. A HP-3562 analyzer was used to compute the transfer function between the fast steering mirror position and the servo error signal while a random excitation was added to the servo error signal. Note the near flat spectrum out to 500 Hz and again the resonance at 800 Hz showing, in this case, as a dip (it can be either a small dip or peak depending on the exact servo filter characteristic).

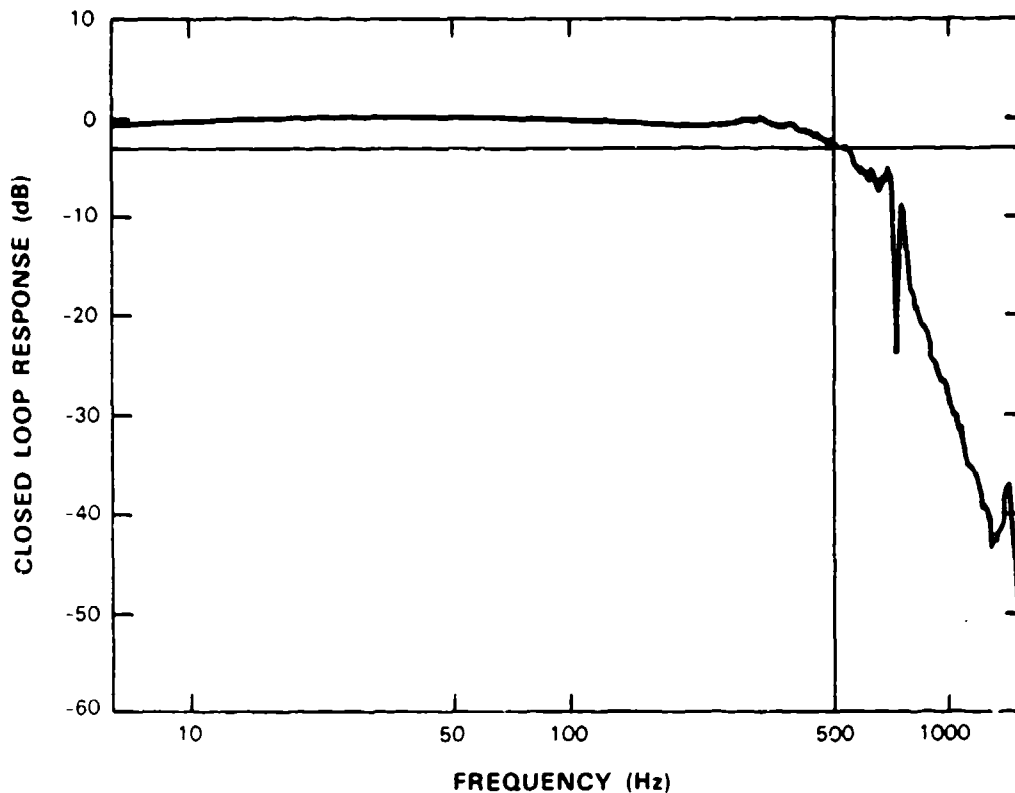
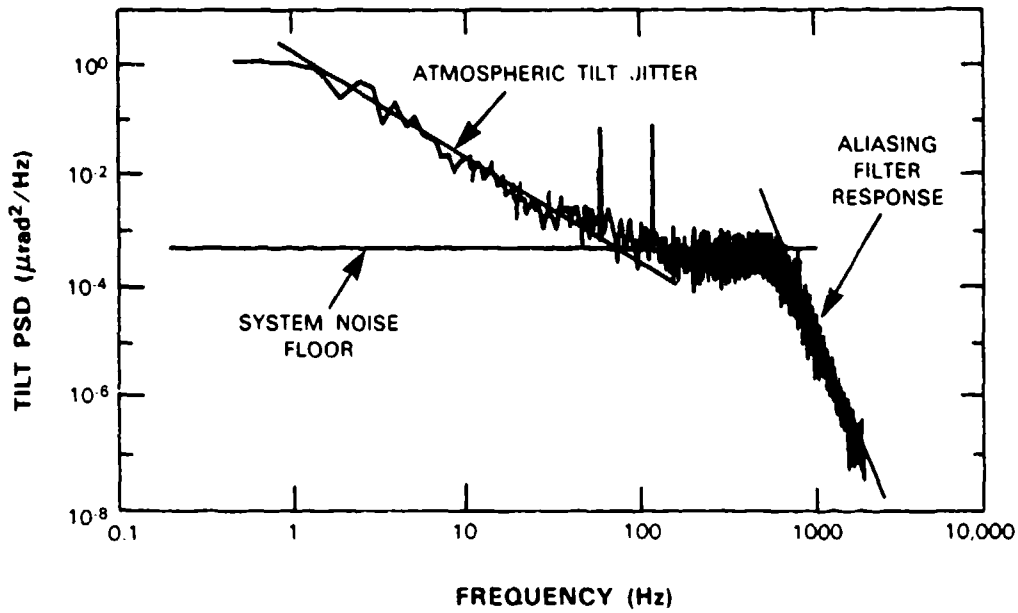


Figure 3-4. Closed-loop response of fast steering mirror in caged mode. Response for azimuth axis is shown; elevation response was similar.

### 3.3 STAR-TRACKING BANDWIDTH CAPABILITIES

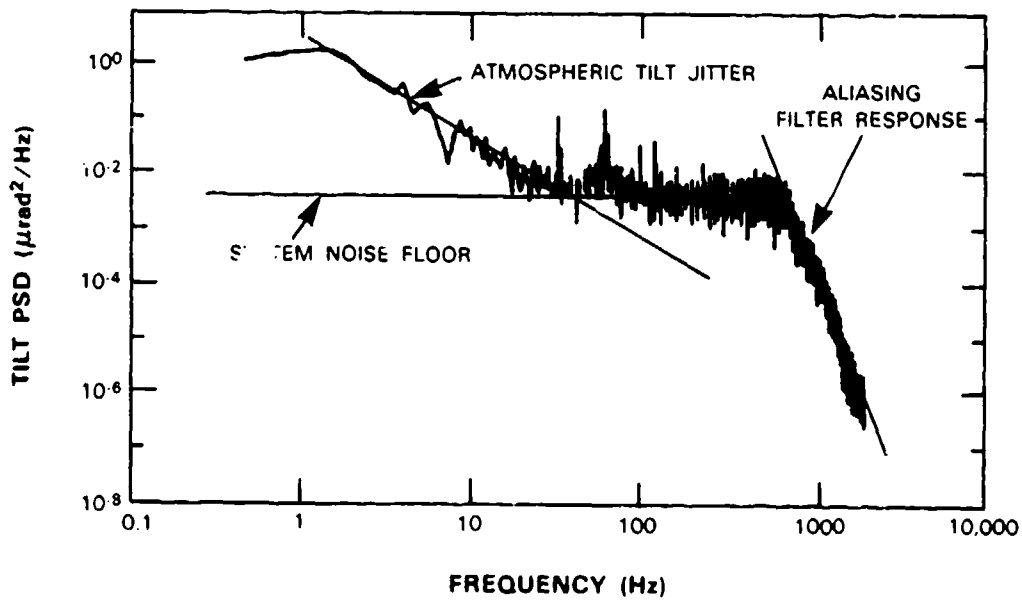
Unlike test sources used to determine ultimate performance, stars are relatively faint and this seriously impacts the measurement bandwidth capability. To determine the usable bandwidth, stars of various stellar magnitudes were tracked and the mirror position and optical error signals were processed for power spectral density plots. By noting the frequency at which the tilt spectrum intercepts the noise floor, for each stellar brightness, the brightness limited bandwidth is determined. Figures 3-5 and 3-6 show the single-axis PSD plots for 2nd- and 4.5th-magnitude stars under similar seeing conditions and elevation angles. The tilt measurement extends to 100 Hz for a 2nd-magnitude star, but only to 40 Hz for a 4.5th-magnitude star.

Initial calculations indicated that we could reach 100 Hz with 4th-magnitude stars, and our disappointment with these test results initiated further study. Among the candidate causes for less than theoretical performance was the value for photomultiplier gain. A careful measurement determined the value to be 9 which was substantially different from the catalogue value of 13. Optical transmission was also too optimistic, measuring slightly more than half of predicted. Because of the large number of surfaces, a few percent per surface makes a large error in total



92839-18

Figure 3-5. Tilt power spectral density on a 2nd-stellar-magnitude star (mirror azimuth position plus residual quad detector error).



92839-19

Figure 3-6. Tilt power spectral density on a 4.5th-stellar-magnitude star (mirror azimuth position plus residual quad detector error).

throughput estimate. In addition, all the reflectance measurements were made with a HeNe laser at 0.63- $\mu\text{m}$  wavelength, but our photomultiplier system has peak response around 0.35  $\mu\text{m}$ . Despite these shortcomings, good measurement capabilities existed and we proceeded with the data-collection task.

### 3.4 CALIBRATION OF THE OPTICAL ERROR SIGNALS

The angle-of-arrival to each of the binary stars was obtained during the double-star measurements by adding the fast steering mirror position and the residual quad detector sensor output. Calibration of both the steering mirror position sensors and the quad detector output signals is important if precise measurements are to be obtained. Although inclusion of the residual errors is unimportant at low frequencies, up to about 20 Hz for a 4th-magnitude star, its importance increases with wide-bandwidth measurements and is essential for data collection beyond 50 Hz.

Since the slope of the quad detector output voltage vs angle error depends on the size of the image on the tip of the pyramid, this transfer curve is dependent on the atmospheric seeing conditions and must be calibrated for the particular seeing conditions during data-taking. This makes it very difficult to accurately determine the angle-of-arrival error implied by the quad detector output and is the main reason why we used a fast steering mirror in front of the detector, so that the bulk of the angle-of-arrival measurement could be obtained from the fast steering mirror position and only a very small portion would come from the quad detector output voltages. If the quad detector error signal is poorly calibrated (because the seeing conditions have changed), it will contribute only a small error to the total measured angle.

The optical error voltage was calibrated with the optical tracker in the caged mode. In this mode, the fast steering mirror was electrically positioned stationary and aligned to the optical axis. Next, a star image was sinusoidally scanned in x and y across the pyramid tip by scanning the Firepond telescope secondary mirror, and the error voltages were recorded. These scan tests employed angle displacements of only a few microradians, since larger scan angles result in a slightly nonlinear output vs angle. A 2nd-magnitude star (Polaris) was the test source for these measurements. The measurement was performed only after the servo gain was adjusted for the particular seeing condition of the test. This ensured a reliable value for the optical error voltage calibration as this parameter is normalized (gain adjusted) before each binary star experiment to take into account night-to-night seeing variations. Often the gain had to be reset in a single night's run, since the seeing often stepped to a new strength level partway through the night.

### 3.5 ANGLE-OF-ARRIVAL CALIBRATION

Precise measurement of the differential tilt magnitude requires an exact calibration of the fast steering mirror LVDT voltage as a function of position. The angle-of-arrival tilt calibration of the fast steering mirror consisted of five separate techniques, each of which was used for angle-of-arrival calibration in various phases of the experimental program. Three of these methods involved active optical tracking, and the remaining tests were of a rather indirect nature.

**Rotating Light Source:**— This test consisted of tracking a rotating light source, a small-filament 6-V clear bulb and attached lantern battery. The assembly was rotated at 7 rps using a small dc motor. The bulb filament center was offset 2.25 cm from the rotation axis, thus producing a circle of  $\sim 10\text{-}\mu\text{rad}$  angular diameter as viewed by the telescope at a distance of 5.4 km. The axis of rotation was accurately aligned with the telescope line-of-sight, producing a true circle of rotation in the telescope field-of-view. Recording and digitizing the peak voltage in each axis (x and y) provided a scale in terms of counts (volts) per microradian in the sky.

**Secondary-Mirror Scans on a Star:**— This method was an active star tracking test with tilts introduced with the calibrated Firepond telescope secondary mirror. Here, the secondary mirror is computer controlled with various optional scan functions such as a circle, raster, or simple x or y motion. These scan motions can be commanded over a wide range of excursions and rates. We operated mostly with a circle to match the rotating light tests.

**Input Focal-Plane Light Source:**— In this test a point source, mounted on a precise x,y,z translation stage, was located at the input focal plane of the tracker package. The plate scale is calculated for this point of the optical system providing a value in terms of  $\mu\text{rad}/\text{mm}$ . While actively tracking the point source, the stage was translated, alternately, in x and in y by  $10\text{-}\mu\text{rad}$  steps and the position voltage was recorded as in the previous tests.

**Optical Magnification:**— The optical magnification method infers the calibration value from the optical magnification and the fast steering mirror calibration. The test involved a photographic measurement of the exit pupil diameter (see optical system description) to obtain the optical magnification. This, when combined with the bench check values of the fast steering mirror (volts per microradian in fast steering mirror space) provides the calibration scale in object space.

**Ray Trace:**— A ray trace of the entire system was made to determine the system magnification which was applied to the bench test scale factors of the fast steering mirror as an additional calibration.

All five techniques agreed well, with a peak error of only 10 percent, and provided a nominal calibration constant of 238 mV  $\mu\text{rad}$  in azimuth and 247 mV  $\mu\text{rad}$  in elevation at the analog-to-digital converter interface. We depended on the rotating light as our fundamental standard of calibration, and adjusted the secondary-mirror scanner values to agree. Routine checks during the experimental program were performed with the calibrated secondary mirror.

### 3.6 TRACKER SCALE-FACTOR BALANCE

The two-axis closed-loop tracking method for the differential tilt measurement required that the two trackers respond identically to identical input wavefront slope variations. To balance the tracker position outputs, the analog gain was adjusted to equalize the outputs during a single-star tracking test in which the secondary mirror was scanned in x and in y at 7 Hz with a peak-to-peak angle of  $20\ \mu\text{rad}$ . A power spectral density of the mirror position was recorded for each tracker axis, and the analog gains were adjusted to produce equal output voltages at the 7-Hz frequency. This method, although providing excellent accuracy for ordinary use ( $\sim 5$  percent), left residuals larger than the 1-percent design goal.

To further refine the tracker balance, the following technique was used. A point source light positioned at the input focus and mounted on an x and y translation stage was adjusted, in turn, to the field extremes with the tracker in closed-loop mode. The digitized values (counts) of the fast steering mirror position for each field position were recorded. Software scaling values were then adjusted and applied to these data to bring both axes to equal counts. The resulting scale factor was used in the data processing.

Active tracking tests of a 2nd-magnitude star demonstrated that this final tuning reduced the residual imbalance, tracker number one minus tracker number two, to a value consistent with the observed system noise floor at frequencies of 100 Hz and above. Figure 3-7 shows the power spectral density of each tracker in a single-star test and the result of subtraction, which of course is a demonstration of the tracker measurement noise floor for that brightness level. The optical error signal was included in all tests and measurements.

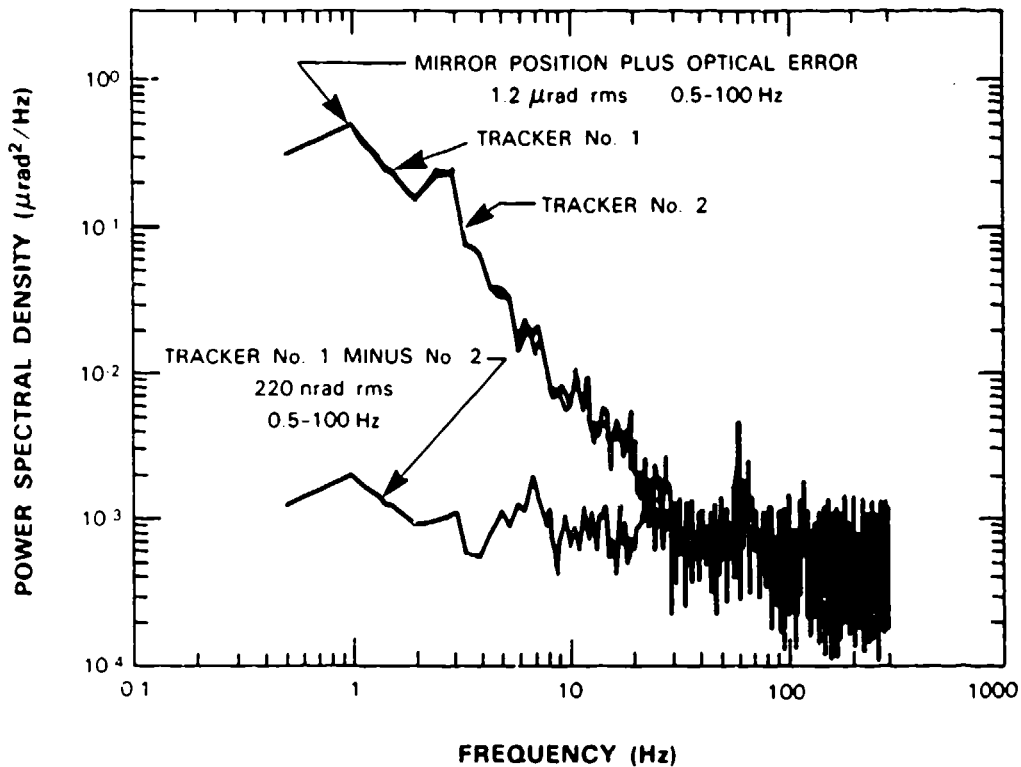


Figure 3-7. Tracker balance while both trackers are tracking the primary star of  $\gamma$  Del. Elevation axis is shown. Note that both trackers have almost the same PSD curve.

## 4. TILT ANISOPLANATISM RESULTS

In this section we will describe the data-collection procedure, give samples of reduced data, and provide the detailed results of the double-star differential tilt measurements.

### 4.1 DESCRIPTION OF AN OBSERVING SESSION

As an introduction to this section, we will describe a typical observing session for the double-star measurement program.

The first task during a session was to adjust the servo gain for maximum bandwidth performance under the prevailing seeing conditions. The telescope was pointed at  $\alpha$ UMi (Polaris) and its image was centered precisely on the wide field-of-view ( $2 \times 3$  mrad) TV monitor viewing through the 60-cm aperture. This pointing usually placed the star within the 300- $\mu$ rad field TV camera viewing through the 1.2-m aperture. Further slight biasing placed the star within the 37- $\mu$ rad field of the tracker. When error signals were observed on an x,y oscilloscope, the automatic track function was engaged. At that time, the narrow-bandwidth mount follow-up servo function was also engaged, which eliminated large steady-state biases during the data taking.

The system was focused by using the normal telescope secondary-mirror focusing controls. Fine focusing was performed while observing the angle-of-arrival difference between the two trackers observing a single star. Because the tracking accuracy improves with a smaller image, the differential tilt of the trackers (while tracking the same star) becomes a minimum at best focus. If the boresights of the two trackers had drifted, a strong dc bias was present in the differential tilt which was corrected by adjusting the optics manually with the bias blocks at their zero (no tilt and  $0^\circ$  roll angle) position. The amplitude of the angle-of-arrival difference signal was minimized by operating the telescope secondary-focus controls.

Next, while tracking Polaris a random noise signal was applied to each tracker's summing junction, and a Hewlett-Packard Model 3562 signal analyzer was used to obtain the servo transfer function and display the servo response. The servo gain was adjusted to flatten the response such that the -3-dB point was at 500 Hz. After this adjustment, narrower bandwidth (10 to 500 Hz) could be obtained by thumbwheel settings. At this point a further refinement of the focus was performed and, if necessary, the transfer curve was run again.

To provide a measure of the seeing, a 1-min sample of tilt tracking was recorded and a twinkle measurement was made using Polaris.

After the Polaris measurement, a double star was selected and brought into the tracker capture field. Since the field stops are sized to accept one component only, either star could be selected for tracking. The adopted procedure was to track the primary (bright component) first, then the secondary. These two tracks were used to determine the tracking noise floor and seeing-induced tilt for each component. Next, the most important test was made, namely tracking each star separately and simultaneously to determine the magnitude of differential tilt. Our standard technique was to first track the primary in tracker number one and companion in tracker number

two. During these operations, an eight-channel strip-chart recorder displayed the mount servo error signals for azimuth and elevation, mirror positions for both trackers, and the mirror position difference for each axis. The analog chart of the difference graphically showed the magnitude of the tilt anisoplanatism effect, it being a peak-to-peak measurement and very dramatic when compared with a single-star track. Next, the role of the trackers was reversed, that is, with tracker number one now operating on the companion. We call this the flip measurement. This was done to detect small differences in the trackers themselves, which could be dealt with later in data reduction. During the double-star measurements, one of the fast steering mirror positions was used to drive the 1.2-m Firepond telescope mount in a low-bandwidth loop, so that the fast steering mirror would not see very low frequencies (less than  $\sim 0.5$  Hz).

This standard measurement set was repeated throughout the night. If a second double rose to a favorable elevation ( $45^\circ$ ), we would switch to the new star to complete the night. Only rarely would more than three pairs be measured in a single night.

## 4.2 DOUBLE-STAR SELECTION

Over one-fourth of the observable stars in our galaxy are binarys. However, for our double-star measurements, the stars must be separated by about  $50 \mu\text{rad}$ , they must be bright and visible at high elevation angles from the Firepond site. In order to have sufficient signal-to-noise for measurements with an adequate bandwidth, a stellar magnitude of 5 or brighter is required, depending somewhat on atmospheric transparency. This consideration reduces the number of candidate doubles to ten that satisfy the necessary brightness and angular separation requirements. For the pairs suitable for observation at our latitude, Figure 4-1 shows the range of

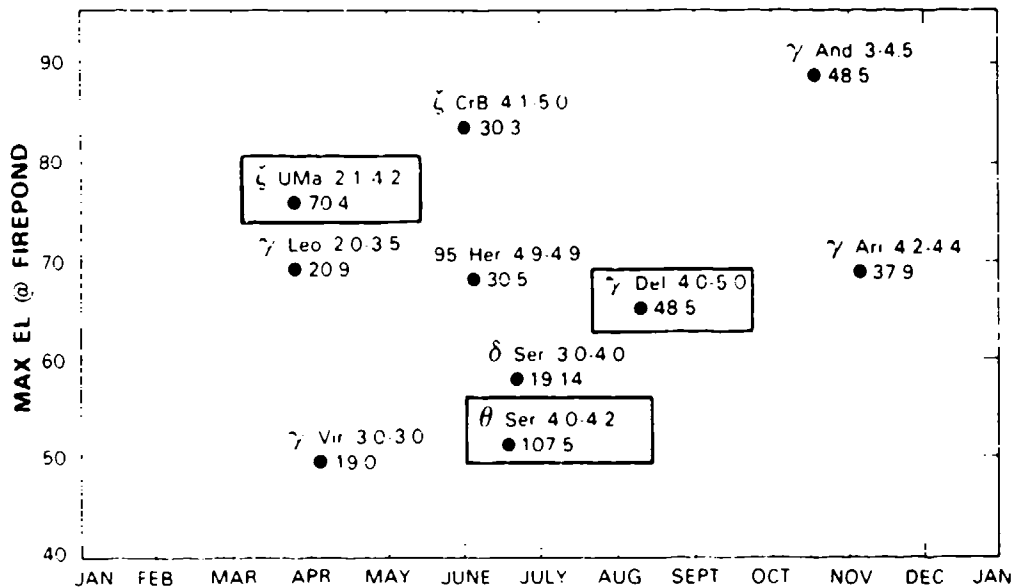


Figure 4-1. Some double stars visible from the Firepond site at various times of the year. The star name is followed by the primary, then the companion, brightness with separation indicated in microradians.

elevations over the course of the year. This report describes the measurements on the three stars identified in the figure. The latest available data for double-star angular spacing in Reference 7 were used; these couples show no appreciable changes during the measurement program period. Couples were chosen with angular separations most closely resembling the lead-ahead angle for low-earth orbits; however, only two pairs have nearly the exact spacing ( $48.5 \mu\text{rad}$  is close to maximum lead-ahead for low-altitude orbits) and other pairs have separations sufficiently dispersed to obtain data on the effect of spacing. We found that the measurement of doubles with spacings simulating geosynchronous orbit lead-ahead ( $\sim 20 \mu\text{rad}$ ) was very difficult and it was possible only on the best seeing nights. This is because the typical seeing blur is usually in the range of  $20 \mu\text{rad}$ ; thus, spillover and tracker pulling by the brighter component simply condemned the effort.

### 4.3 SUMMARY OF DATA RUNS

Table 4-1 lists the measurements which have been analyzed to produce results for this report. Each line of the table corresponds to one measurement on the double star with attendant supporting measurements. The duration of each digital recording was approximately 60 s and consisted of the following:

- (a) Both trackers tracking Polaris providing a measurement of tilt at a constant elevation. These data were used for estimating the atmospheric coherence length during the measurements.
- (b) The control measurements. First, both trackers are pointed at the primary star of the binary pair and data are recorded. This step is repeated with both trackers on the secondary star. These measurements provided an estimate of system noise.
- (c) A data measurement for tilt anisoplanatism. One tracker tracks the primary star, and the other tracks the secondary star.
- (d) A data measurement where the tracker roles are reversed (we call this the "flipped" case).
- (e) A repeat of the first measurement on Polaris.
- (f) Twinkle measurement on Polaris for estimating the isoplanatic angle.

For the data measurements, the orientation of the secondary to the primary is recorded as well as the local temperature, pressure, wind speed, and wind direction. The percent amplitude modulation was measured on Polaris for estimating the isoplanatic angle. We attempted to make all measurements (atmospheric as well as differential tilt) as close in time as possible, but switching back and forth on the stars was quite time consuming and one measurement took close to an hour to complete.

**TABLE 4-1**  
**Summary of Measurements of Double Stars**

DATE	TARGET	TYPE	SEP UPAD	FOI ANGLE DEG	ELEV DEG	TILT (FFD) Z AXIS DEG	DIFF LONG UFAD	DIFF LATN UFAD	DIFF Z AXIS UFAD	CONFERENCE LENGTH (CM)	ISO PLAN ANGLE UFAD
3/17/86	MIZAF	DEL	70	-164	54	2.500	0.715	0.679	0.986	5.530	N/A
3/17/86	MIZAF	FLP	70	-164	54	2.519	0.320	0.878	1.272	5.546	N/A
3/24/86	MIZAF	DEL	70	-175	41	2.566	1.094	0.850	1.385	5.126	N/A
3/24/86	MIZAF	FLP	70	-175	41	2.391	0.326	0.706	1.164	5.305	N/A
3/24/86	MIZAF	DEL	70	-170	47	3.159	0.844	0.889	1.226	4.227	N/A
3/24/86	MIZAF	FLP	70	-170	47	2.861	0.922	0.848	1.252	6.315	N/A
3/25/86	MIZAF	DEL	70	-180	41	3.167	0.553	0.485	0.736	4.215	N/A
3/25/86	MIZAF	FLP	70	-180	41	2.811	0.482	0.474	0.678	5.210	N/A
3/25/86	MIZAF	DEL	70	-165	52	3.461	0.510	0.503	0.716	3.788	N/A
3/25/86	MIZAF	FLP	70	-165	52	2.035	0.415	0.510	0.665	3.961	N/A
4/01/86	MIZAF	DEL	70	-160	51	2.224	0.407	0.370	0.550	6.110	N/A
4/01/86	MIZAF	FLP	70	-160	51	2.295	0.342	0.325	0.472	6.203	N/A
4/02/86	MIZAF	DEL	70	-175	40	2.530	0.921	0.835	1.154	5.059	2.760
4/02/86	MIZAF	FLP	70	-175	40	2.634	0.813	0.651	1.042	5.119	2.396
4/02/86	MIZAF	DEL	70	-168	50	2.831	1.027	0.777	1.292	4.700	2.488
4/02/86	MIZAF	FLP	70	-163	50	2.126	0.528	0.397	0.661	6.267	2.092
5/28/86	MIZAF	DEL	70	01	67	2.017	0.641	0.580	0.864	6.122	0.164
5/28/86	MIZAF	FLP	70	01	67	1.789	0.507	0.487	0.732	8.366	1.475
5/29/86	MIZAF	DEL	70	40	50	1.834	0.521	0.427	0.680	7.810	0.637
5/29/86	MIZAF	FLP	70	40	50	2.205	0.607	0.527	0.810	6.404	0.971
5/29/86	THETA	DEL	107	60	50	1.379	0.724	0.581	0.928	7.884	4.921
5/29/86	THETA	FLP	107	60	50	1.956	0.667	0.461	0.810	7.077	3.704
6/03/86	MIZAF	DEL	70	00	77	1.180	0.746	0.522	0.917	11.40	1.269
6/03/86	MIZAF	FLP	70	-30	37	1.071	0.655	0.413	0.778	15.36	2.194
6/03/86	MIZAF	DEL	70	9	70	1.901	0.526	0.450	0.694	7.601	2.010
6/03/86	MIZAF	FLP	70	3	70	2.010	0.499	0.421	0.653	7.261	1.901
6/04/86	THETA	DEL	107	90	06	2.071	0.855	0.530	1.009	4.374	N/A
6/04/86	THETA	FLP	107	90	41	2.418	0.840	0.555	1.006	5.826	4.631
6/04/86	THETA	DEL	107	90	42	2.823	0.819	0.614	1.022	4.828	N/A
6/04/86	GAMMA	DEL	48	-90	55	2.853	0.583	0.472	0.750	4.777	3.395
6/04/86	GAMMA	FLP	48	-90	55	2.328	0.581	0.444	0.731	4.631	2.646
6/09/86	MIZAF	DEL	70	10	70	1.768	0.770	0.601	0.970	0.485	1.559
6/09/86	MIZAF	FLP	70	10	70	2.017	0.659	0.525	0.842	7.225	1.390
6/09/86	MIZAF	DEL	70	27	64	2.236	0.309	0.349	1.178	6.231	1.326
6/09/86	MIZAF	FLP	70	27	64	1.850	0.575	0.582	0.832	7.992	1.572
6/10/86	MIZAF	DEL	70	40	41	0.309	1.703	1.414	2.214	3.954	2.049
6/10/86	MIZAF	FLP	70	40	41	0.421	1.721	1.400	2.221	3.856	2.643
6/10/86	THETA	DEL	107	60	51	2.491	1.009	0.822	1.601	5.623	2.030
6/10/86	THETA	FLP	107	60	51	2.857	1.152	0.854	1.425	4.770	2.065
6/10/86	GAMMA	DEL	48	-90	59	2.207	0.391	0.428	1.170	6.502	2.050
6/10/86	GAMMA	FLP	48	-90	59	2.049	0.899	0.617	1.492	4.427	0.947
6/10/86	GAMMA	DEL	48	-110	60	2.110	0.717	0.519	0.885	7.271	2.900
6/10/86	GAMMA	FLP	48	-110	60	2.541	0.770	0.550	0.952	5.489	0.966
6/25/86	MIZAF	DEL	70	45	55	2.072	1.182	0.972	1.531	7.014	1.905
6/25/86	MIZAF	FLP	70	45	55	2.179	1.280	1.000	1.625	6.601	1.745
6/20/86	MIZAF	DEL	70	00	65	2.000	1.505	1.110	1.886	4.492	1.252
6/20/86	MIZAF	FLP	70	00	65	2.721	1.159	1.155	1.819	5.058	2.014
6/20/86	MIZAF	DEL	70	40	50	1.997	0.300	0.308	1.200	7.221	2.181
6/20/86	MIZAF	FLP	70	40	50	2.187	1.007	0.858	1.481	6.571	2.294
7/01/86	THETA	DEL	107	50	51	1.026	0.755	0.611	1.006	9.327	2.471
7/01/86	THETA	FLP	107	50	51	1.974	0.781	0.608	1.009	7.401	1.728
7/01/86	GAMMA	DEL	48	-110	60	1.725	0.654	0.405	0.686	8.729	2.070
7/01/86	GAMMA	FLP	48	-110	60	1.819	0.545	0.400	0.674	9.249	2.428
8/25/86	THETA	DEL	107	75	51	1.758	0.757	0.520	0.918	8.542	4.367
8/25/86	THETA	FLP	107	75	51	1.427	0.783	0.647	1.114	10.52	2.959
8/25/86	THETA	DEL	107	59	51	1.087	0.727	0.587	0.911	6.921	2.627
8/25/86	THETA	FLP	107	59	51	1.941	0.854	0.607	0.975	7.581	1.999
9/10/86	THETA	DEL	107	45	48	2.000	0.819	0.748	1.252	6.928	4.412
9/10/86	THETA	FLP	107	45	48	2.179	0.740	0.785	1.480	6.266	5.041
9/25/86	GAMMA	DEL	48	-122	61	1.962	0.450	0.280	0.580	7.482	N/A
9/25/86	GAMMA	FLP	48	-129	61	1.625	0.493	0.380	0.628	4.387	0.514
9/25/86	GAMMA	DEL	48	-141	61	1.521	0.516	0.420	0.671	10.16	2.552
9/25/86	GAMMA	FLP	48	-145	61	1.259	0.420	0.288	0.617	7.569	0.609
9/25/86	GAMMA	DEL	48	-119	51	2.000	0.573	0.528	0.773	7.309	4.057
9/25/86	GAMMA	FLP	48	-128	60	1.058	0.526	0.514	0.727	7.069	5.110
9/25/86	GAMMA	DEL	48	-113	70	1.197	0.630	0.501	0.703	1.044	1.607
9/25/86	GAMMA	FLP	48	-125	61	1.786	0.792	0.561	0.727	9.043	2.552
9/25/86	GAMMA	DEL	48	-145	59	1.763	0.740	0.721	1.044	11.54	2.179
9/25/86	GAMMA	FLP	48	-180	48	1.467	0.527	0.514	0.742	10.41	4.121

#### 4.4 TYPICAL PROCESSING OF RESULTS

Figure 4-2 shows a sample of raw data on the double-star  $\gamma$ Del (48.5- $\mu$ rad separation). These differential tilt strip-chart recordings are obtained in real time as the data are collected and are very useful for quick-look evaluation of data quality. The two trackers make measurements in azimuth (horizontal) and elevation (vertical) axes; the strip-chart recordings show the differential tilt in these two axes for the case of both trackers tracking one star and each tracker tracking separate stars of the pair.

DATE	STAR EL	AZIMUTH AXIS DIFFERENCE		POSITION ANGLE	ELEVATION AXIS DIFFERENCE	
		TRACKING THE SAME STAR	TRACKING PAIR		TRACKING THE SAME STAR	TRACKING PAIR
OCT 1	63°					
OCT 7	41°					
OCT 9	63°					
OCT 16	58°					
OCT 17	62°					

Figure 4-2. Analog chart record of differential tilt measured on  $\gamma$ Del (48.5- $\mu$ rad separation).

92839-7

The chart shows some interesting characteristics of tilt anisoplanatism and the measurement process. First, when both trackers are tracking the same star, the difference between the two trackers is quite small compared with the double-star tilt differences. This small difference is due to the system noise of the two trackers and gives an indication of the measurement accuracy. Second, while the measurements are made roughly at the same elevation angle, the differential tilt between the primary and secondary stars is quite different in magnitude on different days. Most of the time, the differential tilt is much larger than the system noise measured on one star. Third, when the double-star separation direction lines up approximately with the azimuth axes, the azimuth component is larger than the elevation component; however, when the separation direction is  $45^\circ$ , the two components of differential tilt are approximately equal. The theory also suggests that the longitudinal component in the direction of double-star separation should be larger than the lateral component perpendicular to the star separation.

As interesting as these observations are, more detailed quantitative analyses require additional processing. Our double-star tracking data were processed according to the following procedure:

- (1) The data were scaled using the calibration values discussed in Sections 3.4 and 3.5. The tracker mirror positions were summed with their respective optical errors, and the resulting tilt was rotated into longitudinal and lateral components.
- (2) The power spectral density (PSD) of the various tilts was computed and the differential tilt PSD was obtained by subtracting one tracker tilt PSD from the other.
- (3) Average noise spectrum was determined from the primary and secondary control tracks, and subtracted from the differential tilt.
- (4) The rms values of tilt anisoplanatism for the normal and flipped measurements were computed, and the values were entered into a data base for analysis of trends.

Power spectral densities and other data-reduction results have been processed for the measurements listed in Table 4-1. The resulting plots constitute several volumes with all pertinent information so that further analysis can be carried out at a later date if deemed desirable. The remainder of this section shows samples of the above processing steps.

#### **4.4.1 Rotation of Data**

Since the theory predicts that the magnitude of the longitudinal component of tilt anisoplanatism is larger than the lateral component, it is more meaningful to look at the data in two coordinates -- one longitudinal to the double-star separation, and the second lateral to the star separation.

During a measurement, the double-star pair is observed by a TV camera and displayed on a video monitor in the same axis as the quad trackers. The direction of star separation is recorded

from the monitor screen. Another way to determine the angle is to arbitrarily rotate the differential track data to provide the maximum and minimum components. Figure 4-3 shows a plot of the difference between the two resulting components as a function of rotation angle. For this particular data set, the observed angle from the TV screen was recorded to be  $-60^\circ$  which is seen to produce the maximum difference. This type of analysis was conducted on several data runs with consistent results. Since the TV angle data were recorded for each run, the measured horizontal and vertical components of the track data were rotated by this angle into the longitudinal and lateral components.

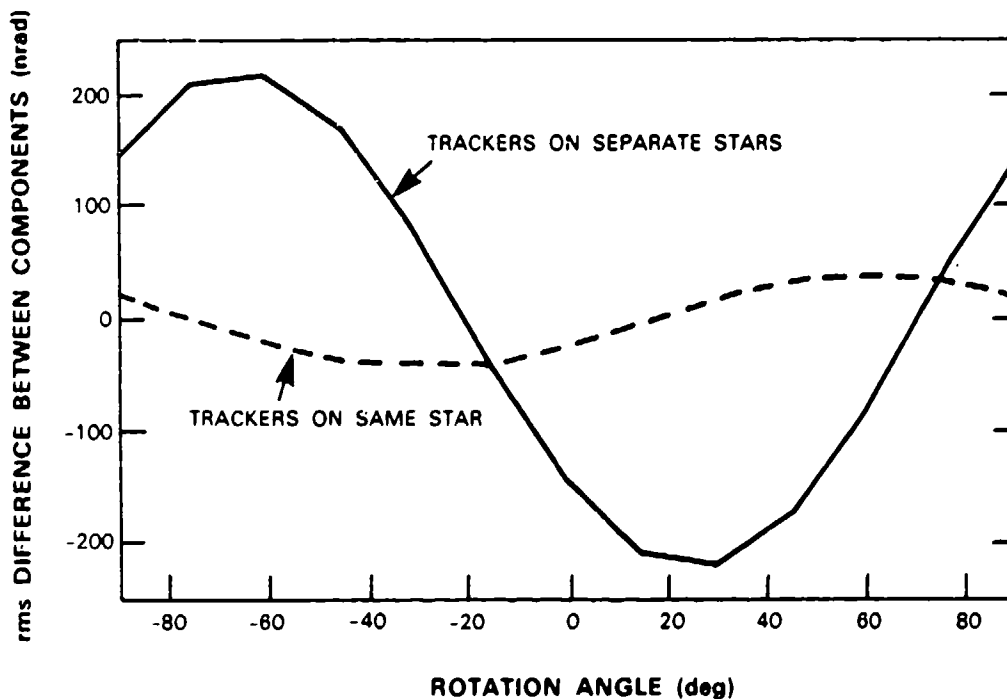


Figure 4-3. Determination of separation direction of double-star  $\gamma$ Del. Note that the correct rotation angle of  $-60^\circ$  provided the largest difference.

Figure 4-3 also shows the difference between the two trackers when they are tracking the same star. The difference is small,  $<50$  nrad, but it changes with the rotation angle. This small difference may be due to statistics, imbalance of the tracker scale factors, or different noise levels in the trackers. Whatever its cause, it is part of the system noise and will be partially compensated by the process of noise subtraction which is described later.

#### 4.4.2 Differential Tilt Power Spectral Densities

After the tracker signals are rotated into the longitudinal and lateral components, power spectral densities (PSDs) of all tracking signals are computed. Observation of the PSD plots out

to 1000 Hz has shown that the system noise starts corrupting data beyond  $\sim 100$  Hz. Because of this, we display most of our PSD plots only out to 100 Hz. Figures 4-4(b) and (c) show the power spectral densities of each tracker for the same time period for the double-star Mizar ( $\zeta$ UMa) on 9 June 1986, 0300 h GMT (Greenwich Mean Time). These and most other power spectral density curves shown in this report are computed over a time period of 30 s by averaging fifteen, 2-s samples. The PSDs in Figure 4-4(a) are for the point-by-point differences of the

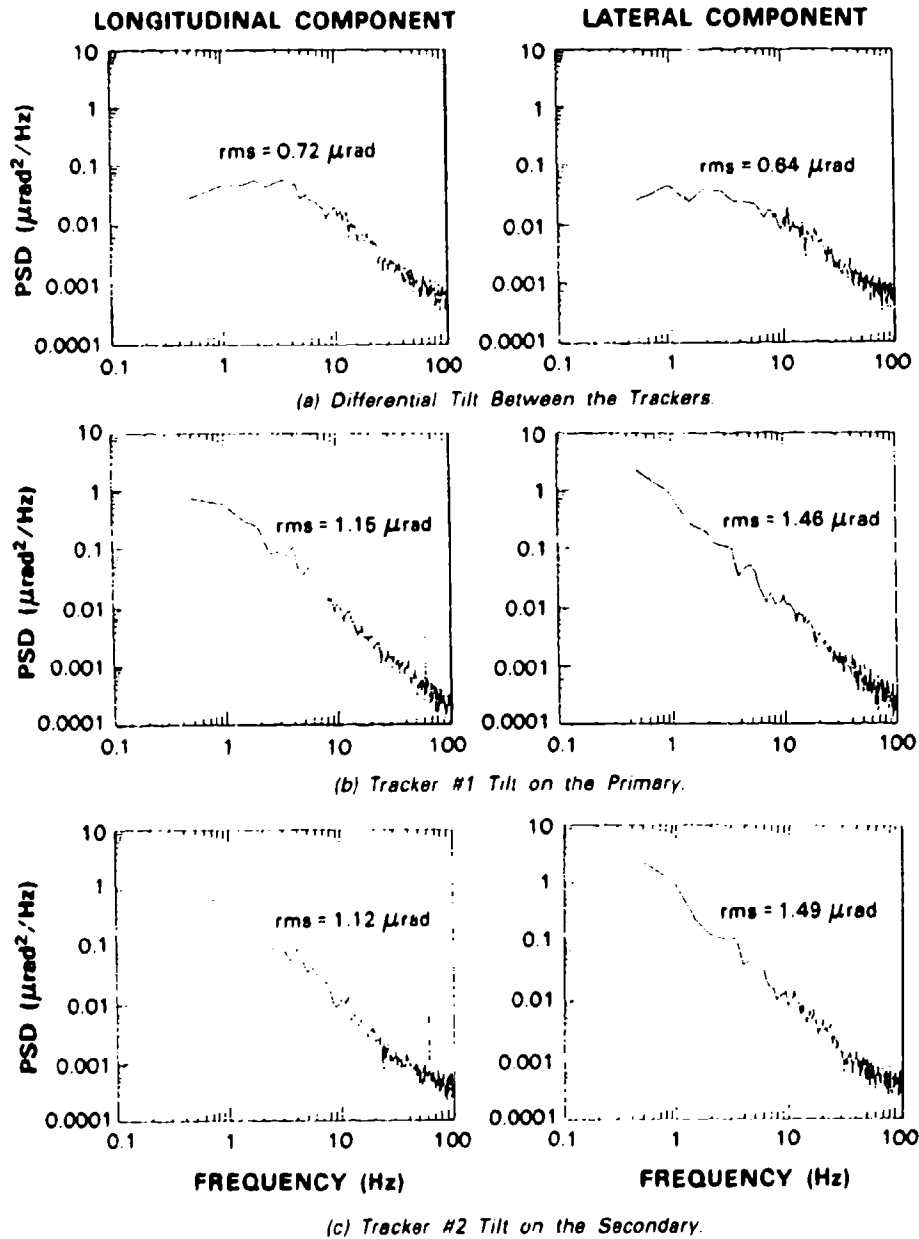


Figure 4-4. Samples of tilt power spectral densities measured on  $\zeta$ UMa (Mizar).

rotated tracker signals. This difference is the tilt anisoplanatism spectrum, and its integral over the frequency domain is the variance of tilt anisoplanatism. Usually, we report the square root of the variance, between 0.5 and 100 Hz, and call it rms differential tilt.

#### 4.4.3 Determination of System Noise

The differential tilt shown in Figure 4-4(a) includes tracker system noise which can be calculated and subtracted to give a better estimate of the tilt anisoplanatism. The system noise is approximated by tracking the primary and secondary stars with both trackers. The differential tilt should be identically zero for these control cases except for the system noise. Even though these noise measurements are made at different times, the system noise should stay the same over short periods of time. Assuming that the system noise is statistically independent of the tilt anisoplanatism, we can subtract the noise PSD directly from the differential tilt PSD. Figure 4-5 shows the noise power spectral density plots for the same Mizar run as shown on Figure 4-4. Because the measured noise during the two control measurements is slightly different, as shown by Figure 4-5, we average the two measurements for subtraction. Subtracting this average system noise of Figure 4-5 from the differential tilt of Figure 4-4(a) gives us a somewhat lower value of tilt anisoplanatism, but hardly any difference is detected in the PSDs when the with- and without-noise curves are overlaid.

#### 4.4.4 Normal vs Flipped Differential Tilt

Since it takes some time (~5 min) to adjust the boresight with the bias blocks, the normal and flipped measurements are made under different atmospheric conditions and sometimes give quite different results.

Figure 4-6 shows the 2-axis rms tilt anisoplanatism for the double-star measurements under normal and flipped conditions. The two values are plotted as a function of measurement number. It can be seen that, while many measurements were close to each other, sometimes tilt anisoplanatism changed considerably during only a few minutes that were required to flip the trackers. Our experience indicated that the change in tilt anisoplanatism was due to atmospheric conditions changing, and was not affected by flipping the trackers. Note that in Figure 4-6 no flip measurements were made for measurement numbers 28 or greater.

### 4.5 MONITORING OF ATMOSPHERIC VARIABLES

Tilt anisoplanatism is strongly dependent on the turbulence profile and, in order to be able to compare theoretical predictions with measurements, it would be desirable to measure the atmospheric structure constant ( $C_n^2$ ) as a function of altitude. Since it is difficult to measure  $C_n^2$  directly, we decided to measure something that would be indicative of the turbulence strength at high and low altitudes. The atmospheric coherence length ( $r_0$ ) and the isoplanatic angle ( $\theta_0$ ) are two integrals of the structure function ( $C_n^2$ ) which weight the structure function with altitude in the following way (Reference 7):

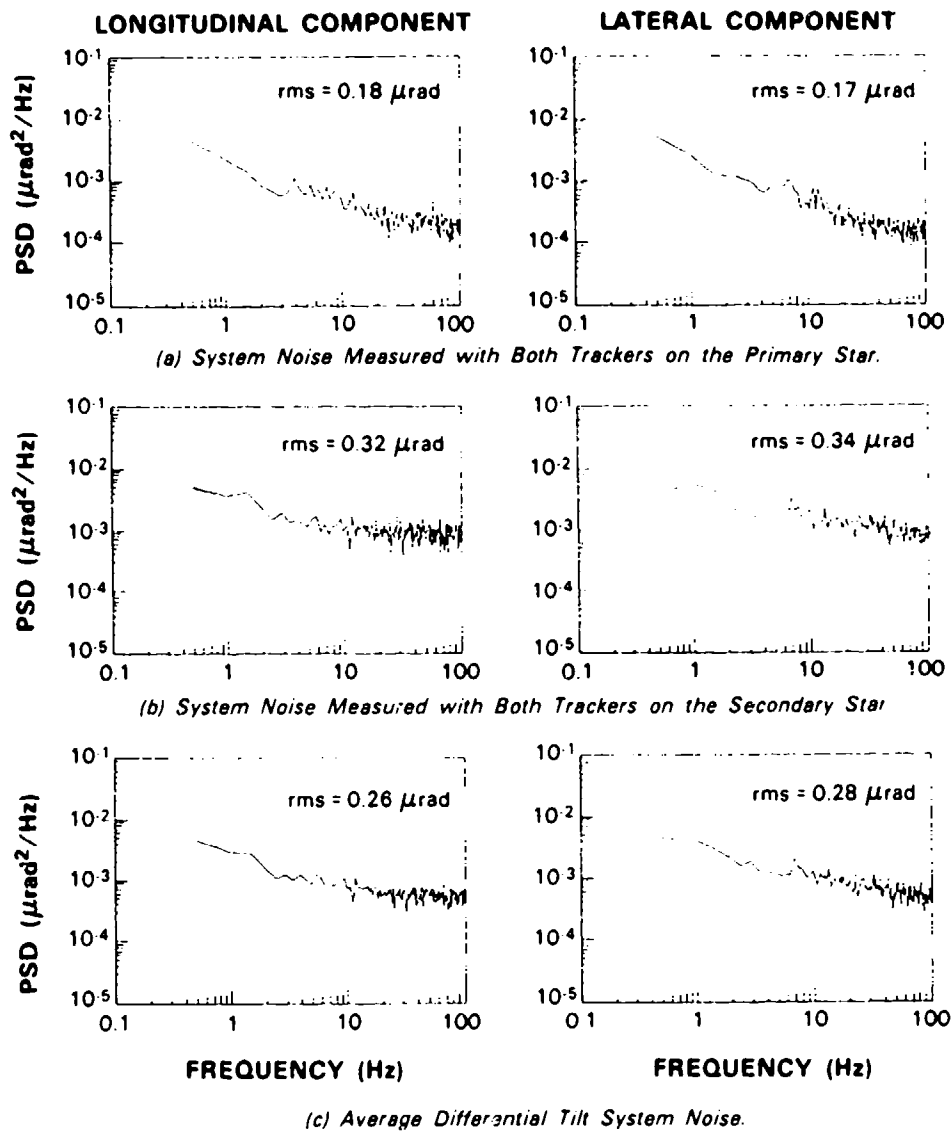


Figure 4-5. Determination of differential tilt system noise on  $\zeta$  UMa (Mizar). Average noise PSD for each component is the sum of the two top curves divided by 2.

104376-7

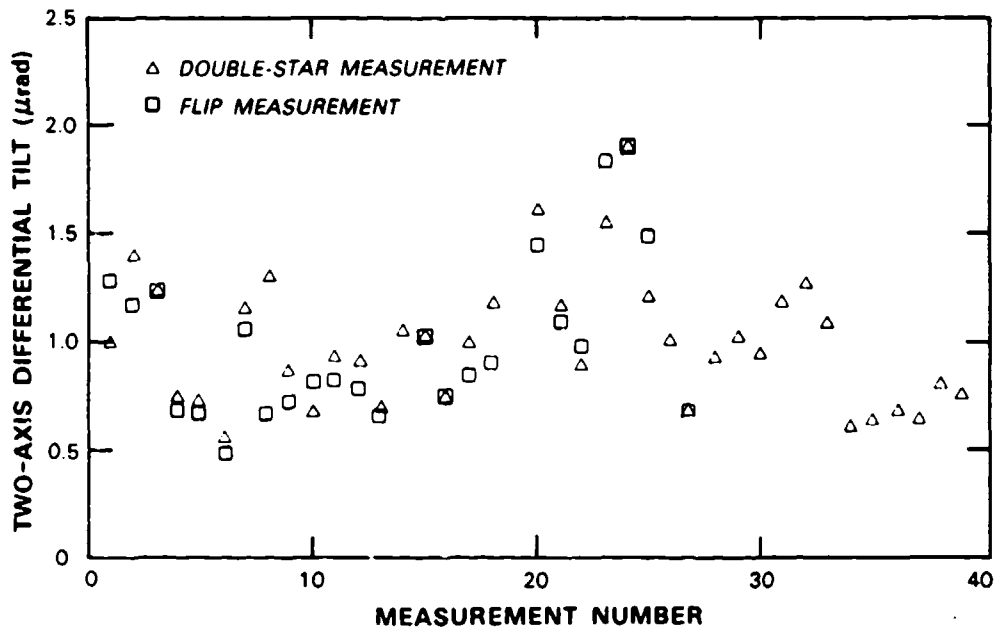


Figure 4-6. Comparison of differential tilt measurements under normal and flipped conditions. Average system noise has been subtracted from the spectra.

$$\text{Coherence length } r_0 = 1.68 [(2\pi/\lambda)^2 \sec \Psi \int_0^\infty C_n^2(h) dh]^{-3/5}$$

and

$$\text{Isoplanatic angle } \theta_0 = 0.528 [(2\pi/\lambda)^2 (\sec \Psi)^{8/3} \int_0^\infty C_n^2(h) h^{5/3} dh]^{-3/5}$$

where

$\lambda$  is the wavelength of light (m),

$C_n^2$  is the refractive-index structure parameter ( $\text{m}^{-2/3}$ ),

$h$  is the altitude above ground,

$\Psi$  is the zenith angle.

Note that the integral in  $\theta_0$  is weighted by  $h^{5/3}$ , but the integral for  $r_0$  is uniformly weighted with altitude. Therefore,  $\theta_0$  is an indicator of high-altitude turbulence and  $r_0$  is more dependent on low-altitude  $C_n^2$ .

Figure 4-7 shows the refractive-index structure function for some of the commonly used atmospheric models. The SLC model was developed for the Submarine Laser Communication System use. The Hufnagel-Valley (H-V) model was initially developed by Hufnagel<sup>8</sup> and later modified by G.C. Valley of Hughes Aircraft Co. Although it is well known that the high-altitude turbulence affects the tilt anisoplanatism the greatest, all models only go to 20-km altitude, above which  $C_n^2$  is assumed to be zero. Ellerbroek and Roberts<sup>9</sup> have calculated the values of coherence length and isoplanatic angle for these models. The values are given in Table 4-2.

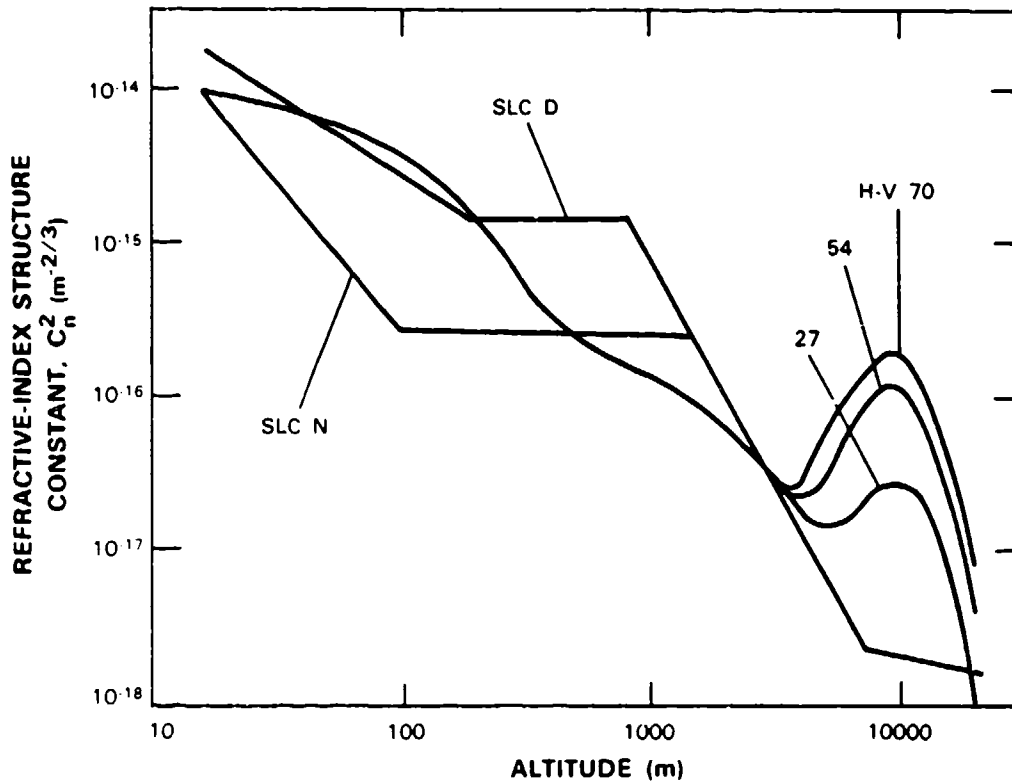


Figure 4-7. Turbulence profiles used for numerical calculations. The numbers listed for the Hufnagel-Valley (H-V) models are the values of a free parameter which is related to the wind speed of the tropopause layer. The SLC N and SLC D are the Submarine Laser Communication System night and day models.

TABLE 4-2		
Atmospheric Parameters for Five Turbulence Models (for $\lambda = 0.5 \mu\text{m}$ , $\Psi = 0$ )		
Turbulence Model	$r_o$ (cm)	$\theta_o$ ( $\mu\text{rad}$ )
SLC Day	5.0	11.8
SLC Night	10.0	12.9
Hufnagel-Valley $v = 27$ m/s	6.4	5.4
Hufnagel-Valley $v = 54$ m/s	5.2	2.4
Hufnagel-Valley $v = 70$ m/s	4.5	1.8

We can estimate the atmospheric coherence length from measurements of tilt jitter to a star. The variance of angle-of-arrival jitter due to atmospheric turbulence is related to the coherence diameter by

$$\sigma^2 = 0.1675 (D/r_0)^{5/3} (\lambda/D)^2$$

where

$D$  is the diameter of the telescope aperture (1.2 m for the Firepond telescope), and

$\lambda$  is the wavelength (peak sensitivity of our photomultipliers is at  $\lambda = 0.35 \mu\text{m}$ ).

While the Firepond measurements are made at  $0.35 \mu\text{m}$ , we can scale the results to  $0.5 \mu\text{m}$  for comparison with calculated values given in Table 4-2. The atmospheric coherence length can be easily calculated from the 1-axis tilt  $\sigma$  by

$$r_0 = 11 \sigma^{-6/5}, \text{ where } \sigma \text{ is in } \mu\text{rad rms and } r_0 \text{ will be in cm for } \lambda = 0.5 \mu\text{m}$$

Figure 4-8 shows the atmospheric coherence length as a function of time of day which was obtained by converting Polaris tracking data to  $r_0$  by the above formula. The time is given in

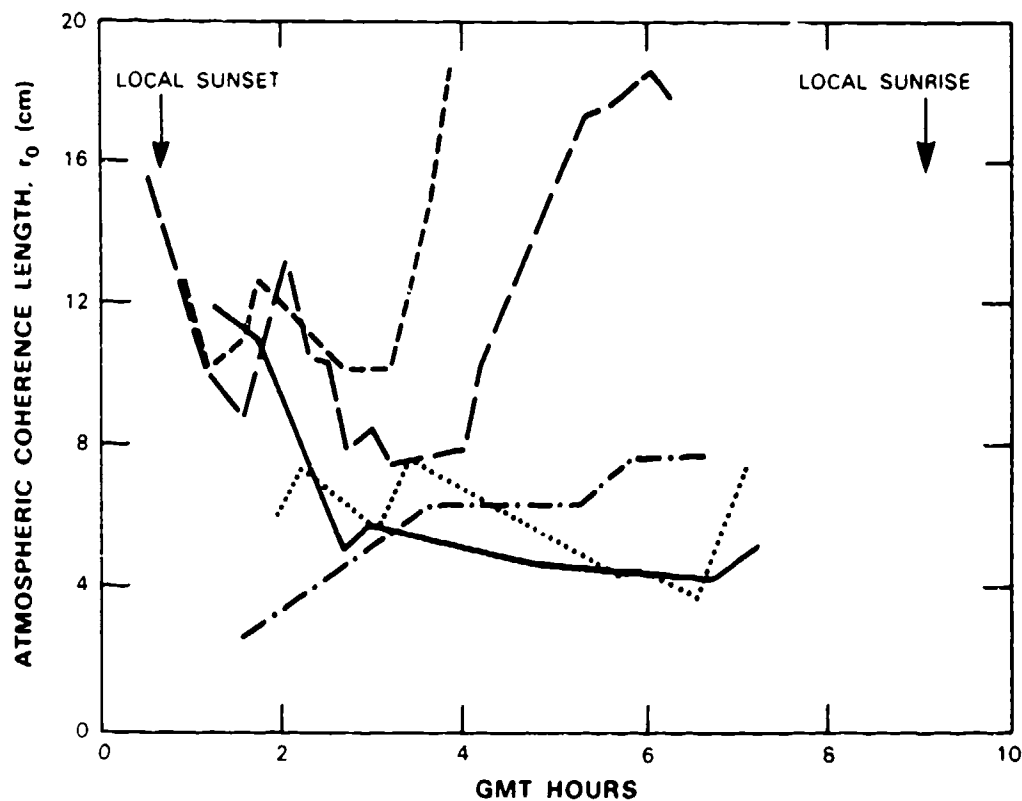


Figure 4-8. Atmospheric coherence length  $r_0$  implied from  $\alpha\text{UMi}$  (Polaris) tilt during five summer nights.

Greenwich Mean Time (GMT) which is 4 h ahead of local daylight savings time in Massachusetts. Thus, the sunset neutral event should occur slightly after 1200 h GMT, i.e., slightly before our measurements.

Loos and Hogge<sup>6</sup> suggested that amplitude scintillations measured with an 11-cm-diam. aperture provide a good estimate of the isoplanatic angle  $\theta_0$ . The instrument which we have built is similar to the one described by Eaton *et al.*<sup>10</sup> of the Atmospheric Sciences Laboratory (ASL), which has been successfully used at White Sands Missile Range for  $\theta_0$  measurements. The instrument measures the percent modulation of the amplitude of the star light. The measured quantity is the percent modulation  $\sigma_s/S$ , which is related to  $\theta_0$  by

$$\theta_0 = K[\ln(1 + \sigma_s^2/S^2)]^{-3.5}$$

where

$\sigma_s$  is the standard deviation of the signal,

S is the average signal amplitude,

K is the calibration constant of the scintillometer (ASL, in Reference 10, has experimentally determined that  $K = 0.9676 \mu\text{rad}$ , and the  $-3/5$  exponent should be 0.6387 for an 11-cm instrument aperture).

The Firepond instrument has not been calibrated against any other instrument, but appears to be working well. The values of  $\theta_0$  which are given in this report were derived by use of the ASL calibration constants which should be applicable to our instrument. Thus, we used the following equation for converting percent modulation to isoplanatic angle:

$$\theta_0 = 0.9676 [\ln(1 + \sigma_s^2/S^2)]^{-0.6387} \quad \text{for } \theta_0 \text{ in } \mu\text{rad for } \lambda = 0.5 \mu\text{m}$$

Figure 4-9 shows the isoplanatic angles determined from the scintillation of Polaris during the measurements. An interesting phenomenon, shown in the figure, is the tendency for isoplanatic angle to reach higher values just before dawn. Although our data base is sparse, this perhaps explains why planetary observers have noted best resolution long after midnight toward dawn! More measurements of this effect are needed since it perhaps indicates a time period where beam pointing experiments are better performed.

#### 4.6. TILT ANISOPLANATISM DATA

The data from all the measurements were collected in a data base and plotted in various forms to get an insight into the trends and nature of tilt anisoplanatism. Here, we show only the tilt anisoplanatism as a function of the atmospheric coherence length and the isoplanatic angle.

##### 4.6.1 Tilt Anisoplanatism vs Atmospheric Coherence Length

Figure 4-10 shows the tilt anisoplanatism data plotted as a function of the atmospheric coherence length  $r_0$ . The value of  $r_0$  was obtained from the total tilt variance of the primary star,

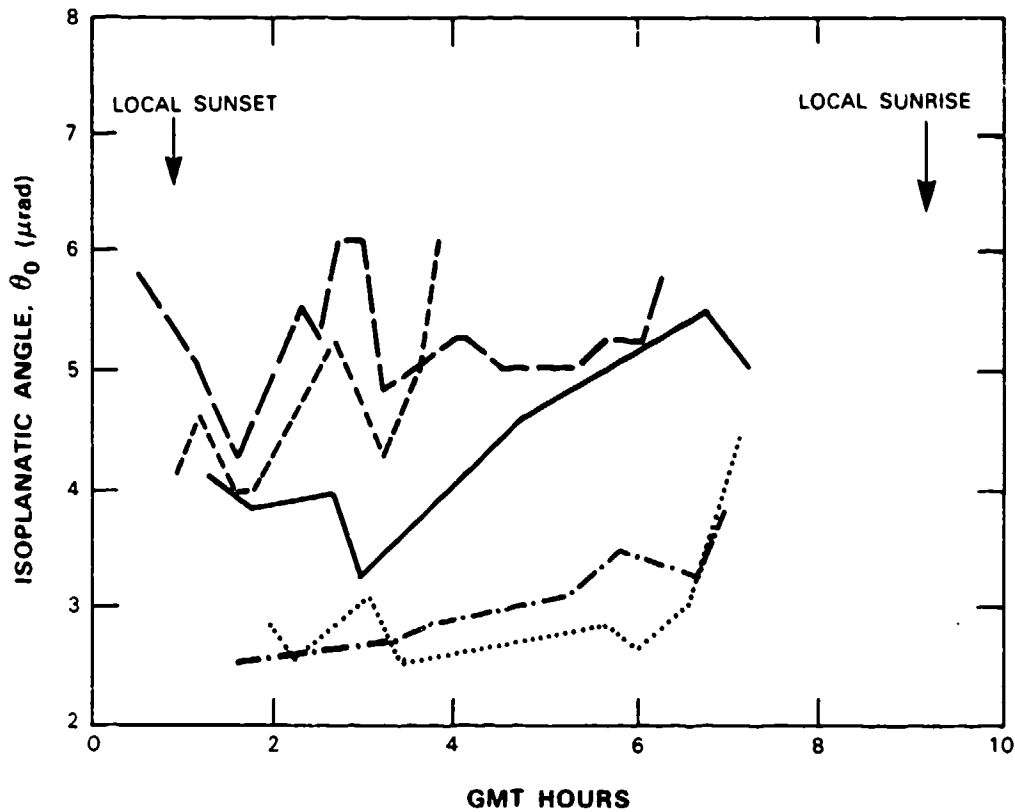


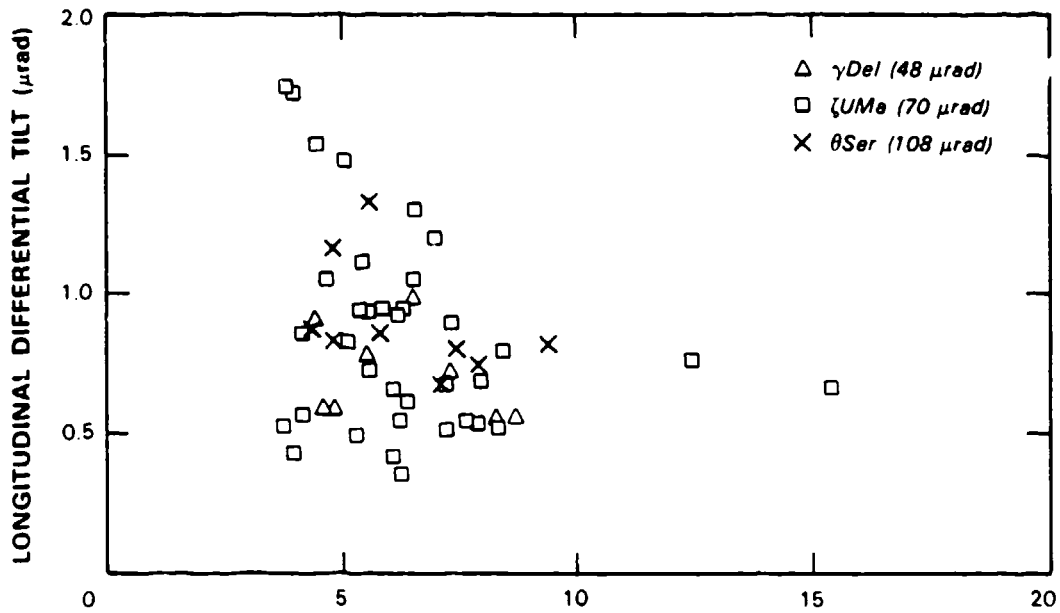
Figure 4-9. Isoplanatic angle  $\theta_0$  at the Firepond site during five summer nights. Obtained from percent amplitude modulation of light from  $\alpha$ UMi (Polaris).

so that the atmospheric coherence length is for the same path and the same time as the tilt anisoplanatism measurements. Data points are shown for double stars  $\gamma$ Del,  $\zeta$ UMa, and  $\theta$ Ser which have quite different separations. The scatter of the data points does not appear to give a clear trend. Even double stars with different separations do not appear to form different data sets.

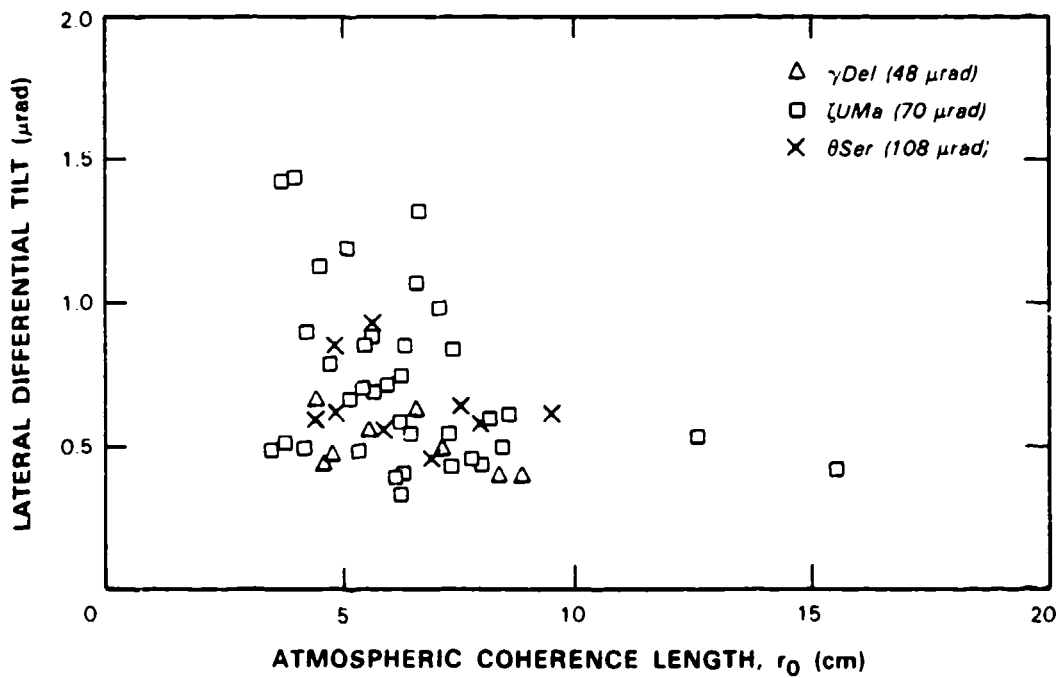
#### 4.6.2 Tilt Anisoplanatism vs Isoplanatic Angle

Figure 4-11 shows a plot of tilt anisoplanatism as a function of isoplanatic angle. Here, the overall trend is somewhat noticeable. As one would expect, the tilt anisoplanatism is much larger for smaller isoplanatic angles. The isoplanatic angle for this curve was derived from the Polaris measurements, by adjusting the isoplanatic angle according to the  $\sec \Psi$ , where  $\Psi$  is the zenith angle to the star on which the differential tilt was measured.

In general, this plotting procedure produced no clear trends in these data sets. It was decided that the data had to be adjusted according to theoretically predicted formulas to reduce scatter.

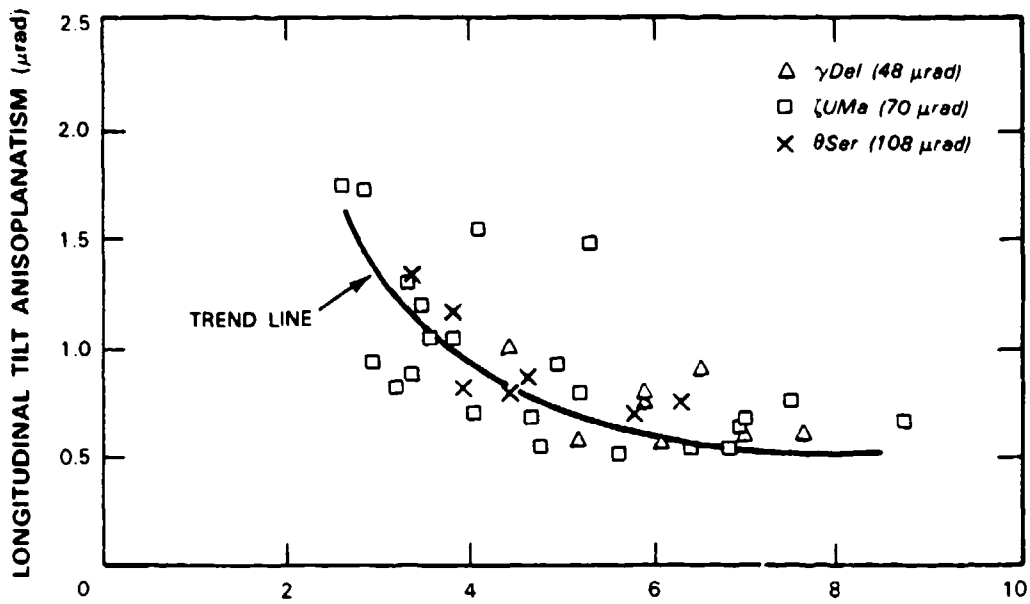


(a) Longitudinal Component.

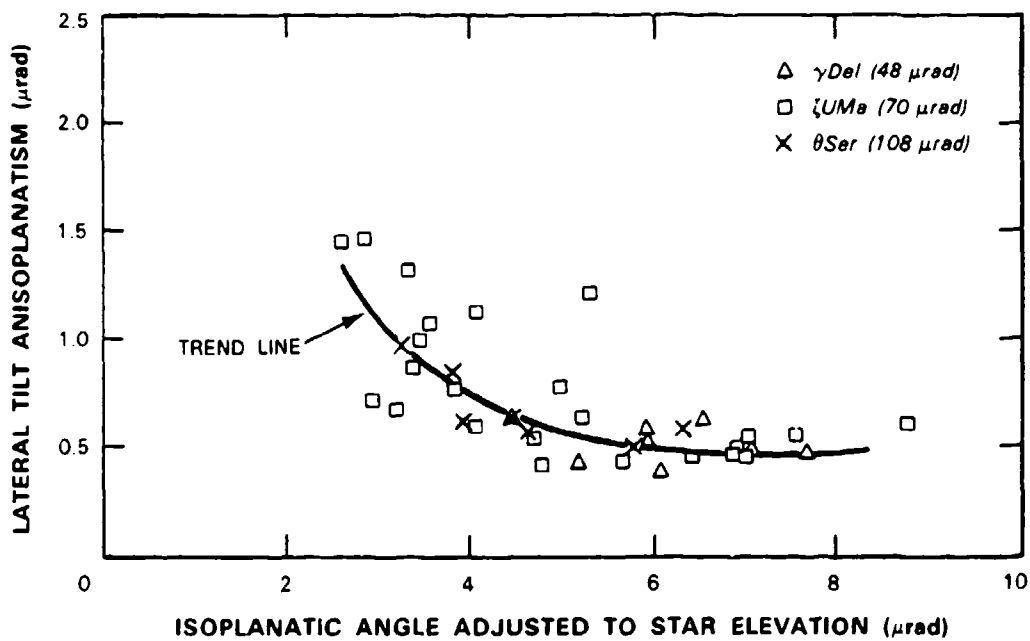


(b) Lateral Component.

Figure 4-10. Differential tilt as a function of atmospheric coherence length. Note that the data are for three double-star separations but data for each star do not follow a separate trend.



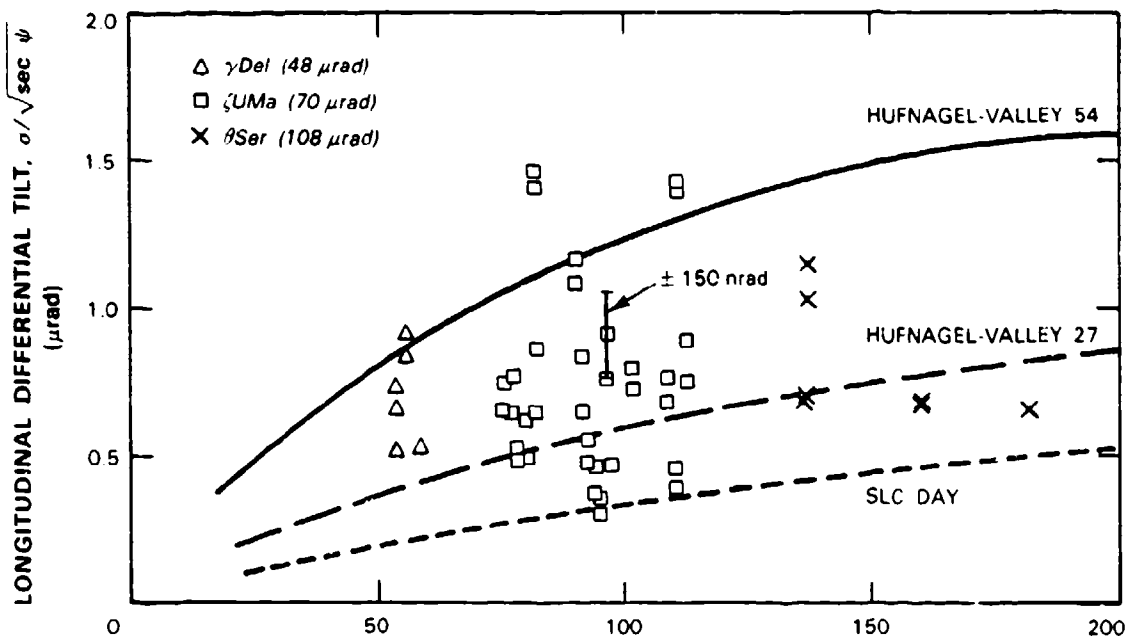
(a) Longitudinal Component.



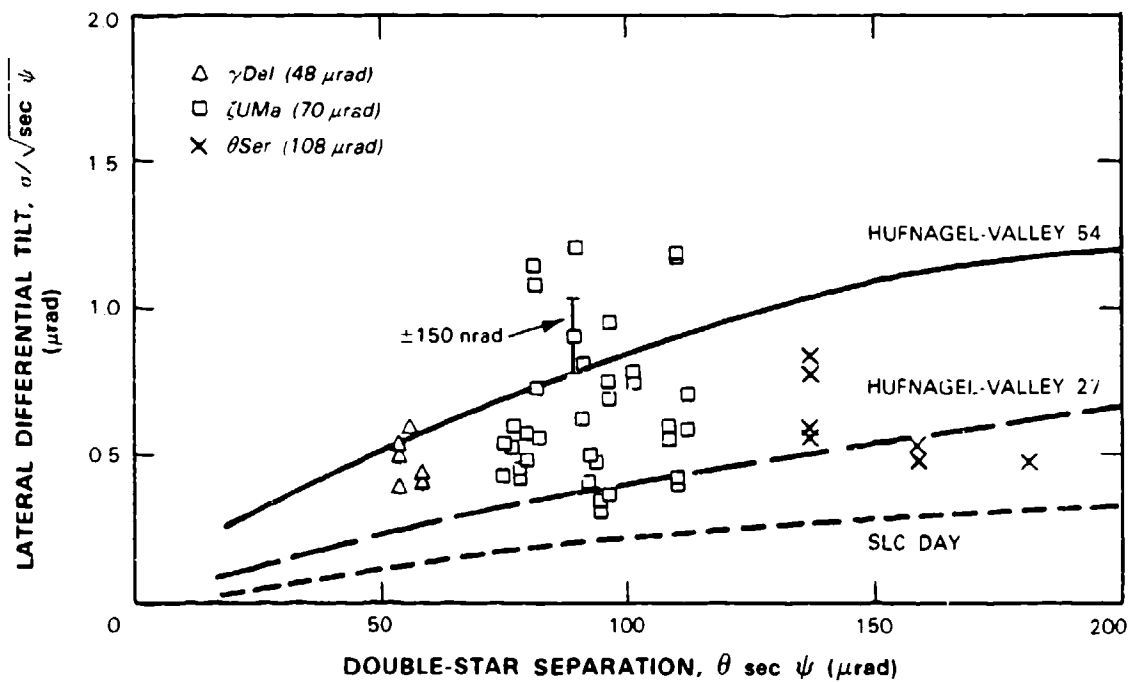
(b) Lateral Component.

Figure 4-11. Tilt anisoplanatism as a function of isoplanatic angle. The trend line was drawn by eye to point out the trend that the data appear to follow.

104376-11



(a) Longitudinal Component



(b) Lateral Component

Figure 4-12. Tilt anisoplanatism as a function of path separation compared with calculations based on several atmospheric models. The measurement accuracy is estimated to be less than the indicated 150 nrad.

## 4.7 COMPARISON OF FIREPOND DATA WITH THEORY

While the theory of tilt anisoplanatism is new, several individuals have performed calculations predicting the magnitude of tilt anisoplanatism. We contracted with the Optical Sciences Co. (tOSC) to make specific predictions of differential tilt for the Firepond 1.2-m telescope and non-rotating quadrant detectors. This report will not describe their theoretical results, but will simply show the tOSC numerical calculations in comparison with the Firepond measured data. More detailed information on tOSC work can be found in their reports which are referenced herein. B. Ellerbroek has shown mathematically<sup>11</sup> that a quad detector approximately measures G-tilt (the aperture averaged gradient of the wavefront) rather than Z-tilt (the best-fit plane to the measured wavefront). Reference 12 shows that the difference between what a null-tracking quad like ours measures and G-tilt is more than an order-of-magnitude lower than differential tilt under an interesting range of parameters. Accordingly, all the other tOSC calculations shown in this report are G-tilt values.

### 4.7.1 Tilt Anisoplanatism vs Double-Star Separation

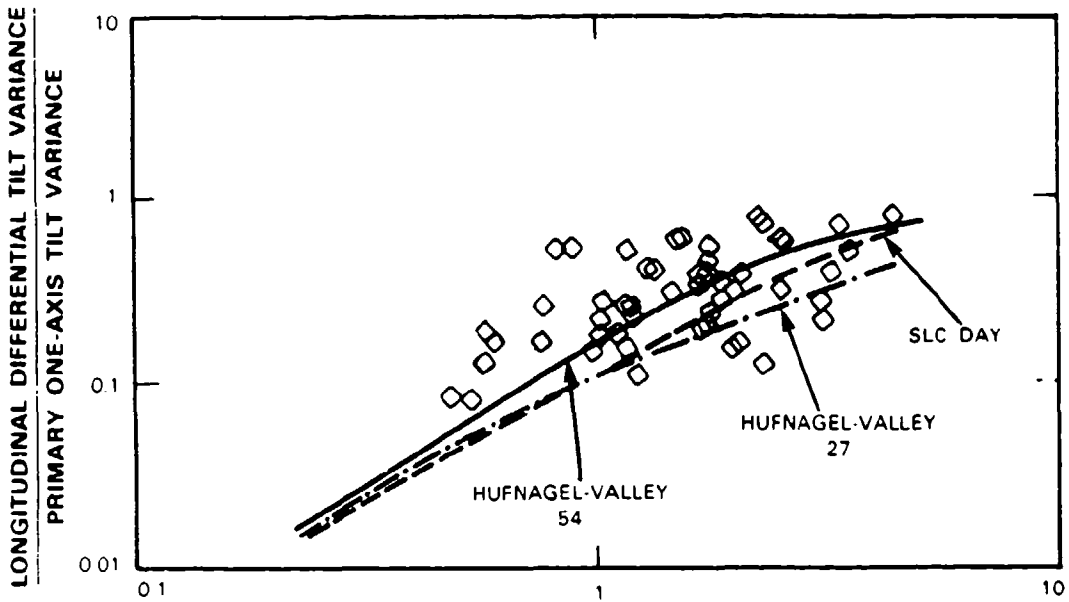
When normalizing the tilt anisoplanatism and the double-star separation by the sec  $\Psi$  functions, one obtains the curves of Figure 4-12. The figure also shows computed curves for three atmospheric models which appear to bracket the measured data. The SLC Day model appears to be the lower bound of our nighttime measurements. Because tilt anisoplanatism is a high-altitude phenomenon, and because the SLC Day and Night models are the same at high altitudes, the SLC Night model is not shown on the figure but would fall on top of the SLC Day curve. The Hufnagel-Valley models have a free parameter which can be adjusted to provide any strength turbulence one wishes at high altitudes. For these data, the Hufnagel-Valley 54 model appears to bracket the data on the high side, except for a few anomalous points.

The theoretical computations are made using the atmospheric models described in Section 4.5. The calculations assumed that the atmospheric structure constant vanishes above 20 km altitude. H. Praddaude<sup>13</sup> has shown that, when these atmospheric models are used to calculate tilt anisoplanatism, the contribution at 20 km altitude is important. R. Sasiela<sup>14</sup> has extended the models to include turbulence above 20 km and has obtained ~25-percent higher values of tilt anisoplanatism than computed by tOSC.

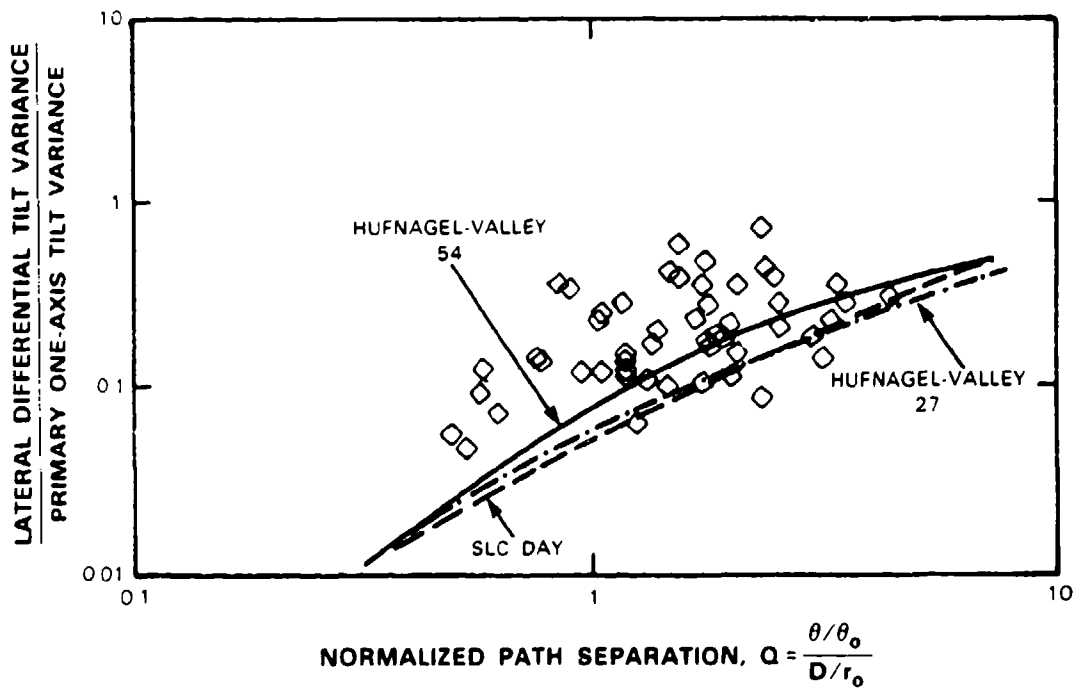
Some data values appear to be anomalous on Figure 4-12. We don't believe this to be a measurement problem; instead, during these measurements, unusual atmospheric conditions persisted. In some cases, the image of the star was very small but danced around with an unusually large magnitude. Other times, the image was quite stationary but its size rapidly pulsed. We attribute these phenomena to unusual high-altitude atmospheric conditions which are not well understood, but were encountered during our measurements on several occasions.

### 4.7.2 Tilt Anisoplanatism vs Normalized Separation

So far, we have plotted the tilt anisoplanatism data in various forms and have used the atmospheric models to compute theoretical curves which show that the measured data are reasonable if particular "standard" atmospheric conditions are assumed. During the measurements, we



(a) Longitudinal Component.



(b) Lateral Component.

Figure 4-13. Tilt anisoplanatism as a function of path separation normalized to atmospheric coherence length and isoplanatic angle. Data points compare favorably with the theoretical computations using several atmospheric models.

also obtained estimates of isoplanatic angle and the atmospheric coherence length, which can be used in predicting the magnitude of tilt anisoplanatism. Glenn Tyler of tOSC has computed the normalized variance of tilt anisoplanatism for the Firepond telescope as a function of atmospheric and system parameters, shown in Figure 4-13, for the SLC and Hufnagel-Valley  $C_n^2$  models (see Reference 9 for details of similar calculations). We also plot the Firepond data on the same figure, where the vertical axis shows the differential tilt normalized to the total angle-of-arrival tilt, and the horizontal axis shows the value of  $Q$  which is defined as follows:

$$Q = \frac{\theta / \theta_0}{D / r_0}$$

where

$\theta$  is the star separation,

$\theta_0$  is the isoplanatic angle,

$D = 1.2$  m is the diameter of the telescope aperture,

$r_0$  is the atmospheric coherence length.

When the data are normalized in this manner, all models collapse to the same curve for weak turbulence levels or small separations. The values of  $\theta_0$  and  $r_0$  which were used in Figure 4-13 were measured just before the differential tilt measurements. The isoplanatic angle was measured on Polaris and was adjusted to the double-star's zenith angle.

#### 4.7.3 Longitudinal vs Lateral Component Magnitude

The two components of tilt anisoplanatism are of different magnitude. Comparison of the theoretical curves of Figures 4-13(a) and (b) and computations by others show that for small separations or weak turbulence conditions the longitudinal component of tilt anisoplanatism in the direction of the double-star separation is larger than the lateral component in the perpendicular direction by a factor of square root of 3. For stronger turbulence and larger separation, the ratio becomes smaller, until at very large separations the two components of tilt anisoplanatism become equal. Figure 4-14 shows the ratio of longitudinal component divided by the lateral component for our measurements; it also shows the range of values which would be expected from the actual double-star separation and the measured atmospheric conditions. Clearly, the measured values are lower than theory predicts, indicating stronger turbulence than the models.

#### 4.8 POWER SPECTRAL DENSITY OF THE DIFFERENTIAL TILT

The power spectral density of tilt anisoplanatism is dependent on the cross wind along the line-of-sight, particularly at high altitudes. In order to predict the differential tilt spectrum, the wind velocity has to be known precisely. During our measurements we had no way to measure the wind-velocity profile. Instead, we relied on the US Weather Service to provide us that information. Unfortunately, the nearest weather stations to Firepond are in Albany, NY; Portland, ME; and Chatham, MA. The Firepond facility is roughly equidistant from all three stations, as shown on the area map of Figure 4-15.

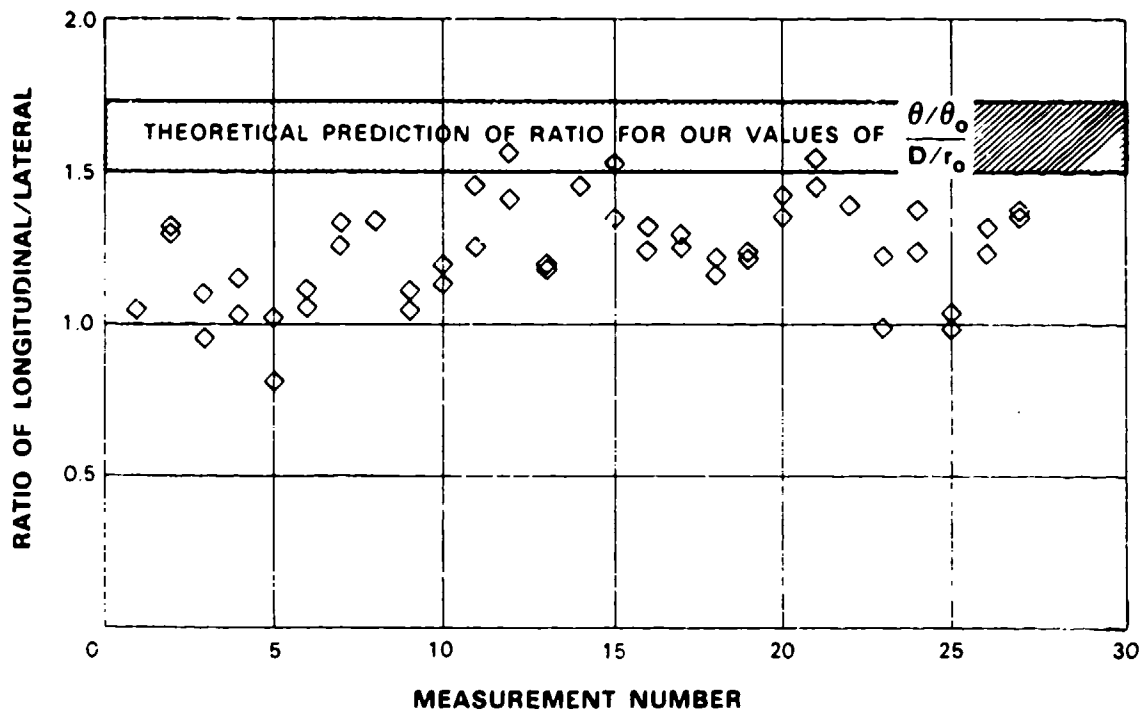
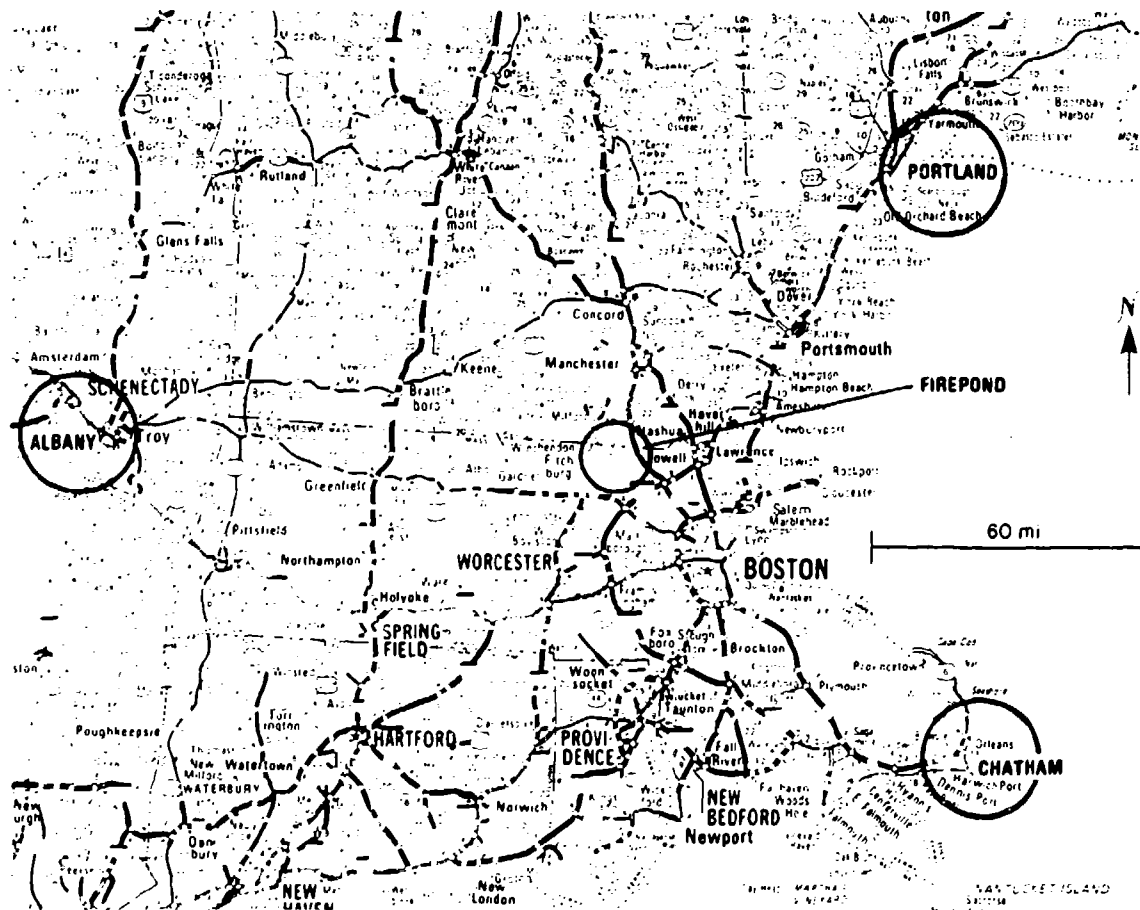


Figure 4-14. Ratio of longitudinal and lateral components of tilt anisoplanatism for Firepond data.

104376-14



104376-15

Figure 4-15. Location of Albany, Portland, and Chatham weather stations with respect to Firepond.

Figure 4-16 shows the wind profiles with altitude above the mean sea level for the three sites for 10 June 1986 taken at 0 h GMT. As can be seen, the three sites had similar wind profiles, particularly at high altitude. We used the Portland data as being valid at Firepond during the whole evening of measurements. The actual winds at Firepond were probably quite different at lower altitudes, so the theoretical calculations should not be taken too seriously.

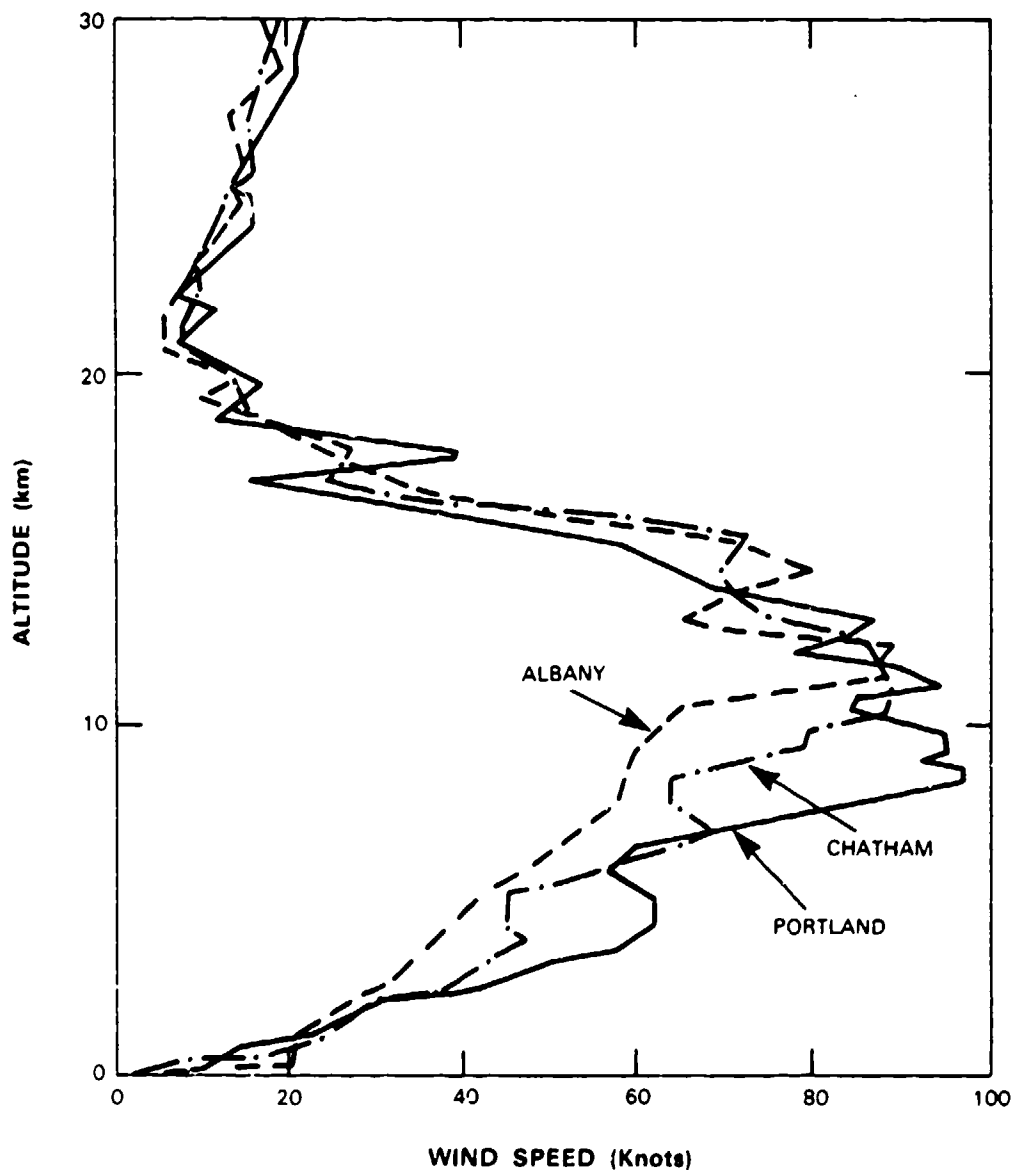


Figure 4-16. Wind profiles at Albany, Portland, and Chatham during the evening of 10 June 1986, 0 h GMT. Wind direction was approximately from the north at all stations. The values for Portland were used for predicting power spectral densities at the Firepond site.

The Optical Sciences Co. performed calculations valid for the actual elevation angle to the double star and detailed wind as measured by the Weather Service at Portland. The wind was assumed to be in the horizontal direction with zero vertical components. Figure 4-17 shows the calculated frequency spectra for various atmospheric models. These 2-axis PSD curves are for the double-star Mizar with a separation of  $70 \mu\text{rad}$  at an elevation angle of  $73^\circ$ . While agreement between the measurements and calculations is quite good, we must point out that the shape of PSD curves changed substantially from one measurement to the next.

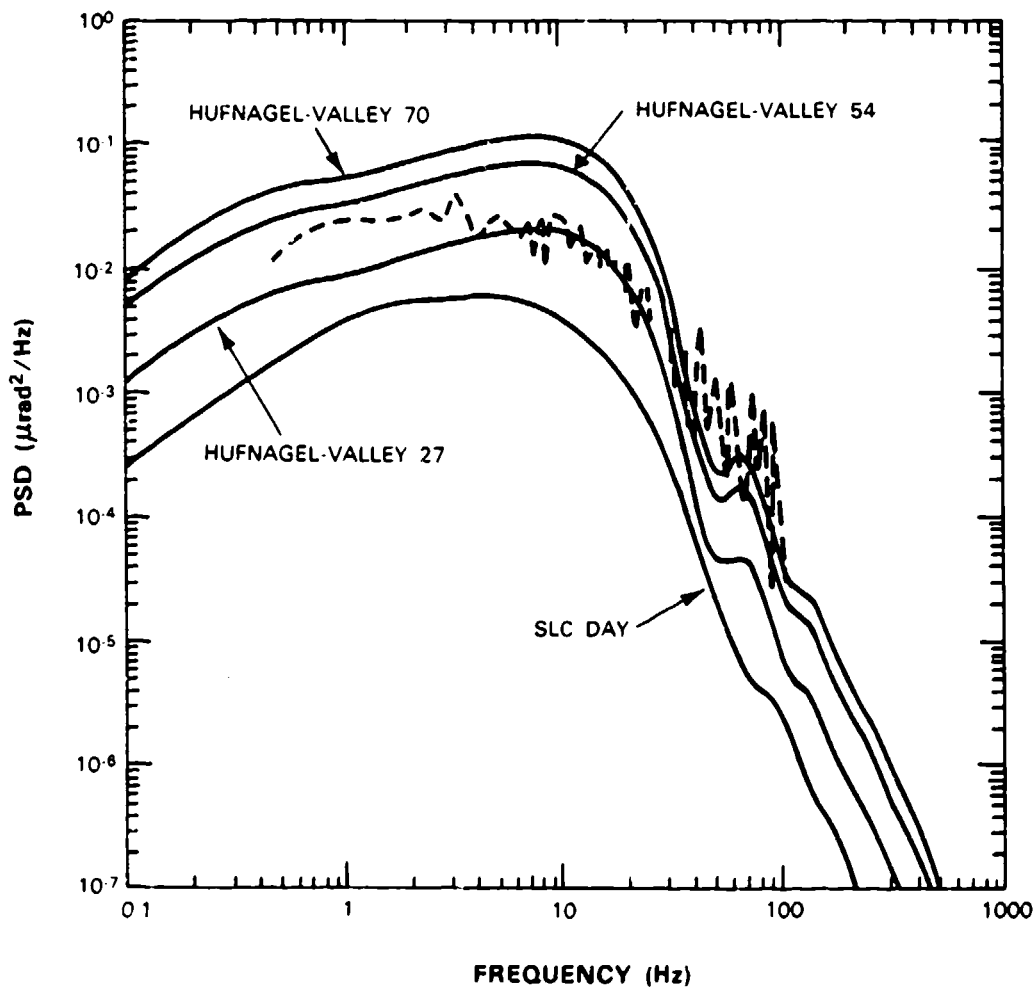


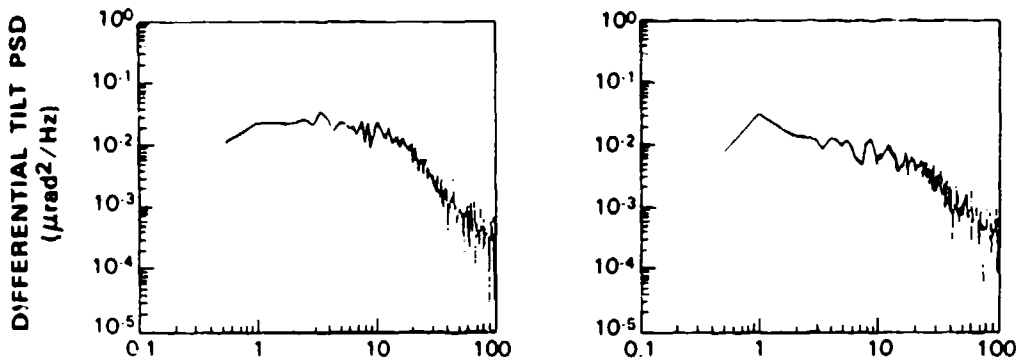
Figure 4-17. Power spectral density of total differential tilt of  $\zeta$  UMa (dashed curve) on the evening of 10 June 1986 (02:11:16 GMT) compared with theoretical calculations.

104378-1F

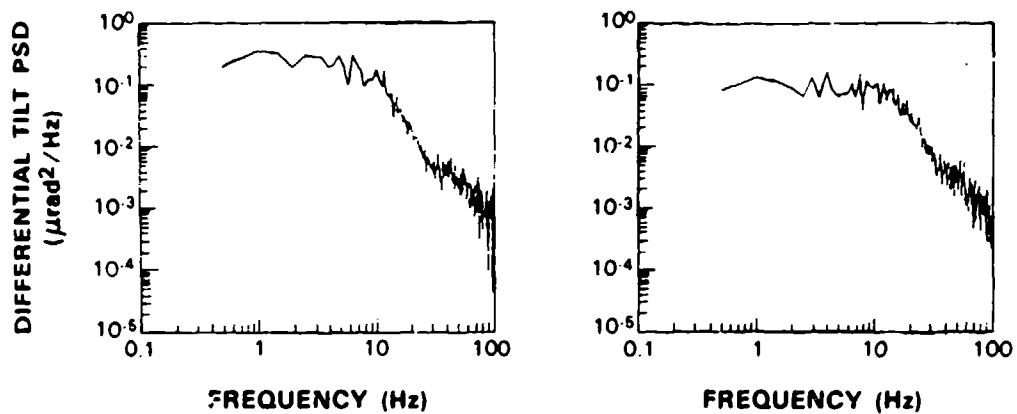
Figures 4-18 and 4-19 show some samples of power spectral densities taken during the same evening. We assume that the winds stayed the same during the whole evening, so that the differences in the shape of the PSD curves are due to different atmospheric seeing conditions and perhaps the elevation angles.

Figure 4-18(a) shows the longitudinal and lateral components of the power spectral density for reasonably benign conditions. The rms tilt anisoplanatism was well below  $1 \mu\text{rad}$ . In Figure 4-18(b) we have the power spectral densities for the same star (Mizar) when the tilt anisoplanatism was well above  $1.5 \mu\text{rad}$ . We note that for the higher tilt anisoplanatism case, the low frequencies increase by almost a factor of 10 and also the hump at  $\sim 60 \text{ Hz}$  which was predicted by the theoretical curves starts appearing.

Figure 4-19 shows the shape of the spectra for three double-star separations. The spectra are quite different for the different separations; however, it is not clear whether the shape changes because of the star separation or because of some other condition which has changed. Note that the magnitude of the tilt anisoplanatism is quite different for Figures 4-19(a), (b), and (c). From these limited samples and many others that were collected at Firepond, one must conclude that the shape of the PSD curves can be highly variable. For strong tilt anisoplanatism, most energy is below 20 or 30 Hz and drops off rather quickly. While our system was not able to measure tilt anisoplanatism beyond 100 Hz, the lower-frequency PSD curves appear to indicate that the tilt anisoplanatism energy is negligible above 100 Hz.



(a) 02:11:16 GMT — Longitudinal (Left) and Lateral (Right) Components Are 0.56- and 0.53- $\mu\text{rad}^2/\text{Hz}$  rms, Respectively.  $r_o = 7.2 \text{ cm}$ ,  $\theta_o = 4.3 \mu\text{rad}$ , Elevation =  $73^\circ$ .



(b) 05:55:46 GMT — Longitudinal (Left) and Lateral (Right) Components Are 1.7- and 1.4- $\mu\text{rad}^2/\text{Hz}$  rms, Respectively.  $r_o = 3.9 \text{ cm}$ ,  $\theta_o = 4.5 \mu\text{rad}$ , Elevation =  $42^\circ$ .

Figure 4-18. Typical power spectral densities taken during the evening of 10 June 1986 on the double-star  $\zeta \text{UMa}$  (Mizar).

104376-17

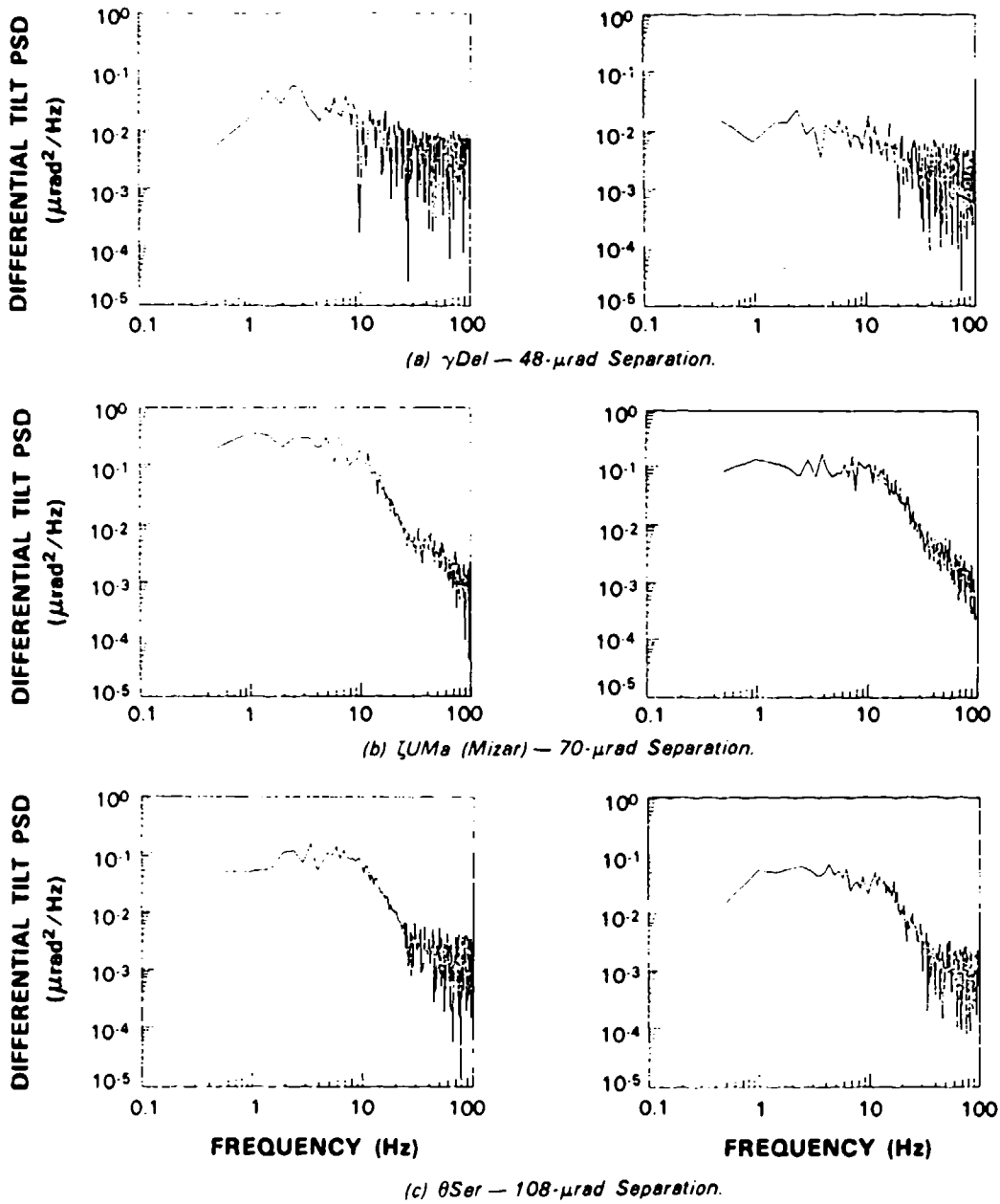


Figure 4-19. Power spectral density for three double-star separations for longitudinal (left) and lateral (right) components during the evening of 10 June 1986.

## 5. CONCLUSIONS

The magnitude of tilt anisoplanatism as a function of angular separation has been measured with the Firepond telescope and two precise optical trackers. The precision of the measurements was demonstrated to be sufficiently fine to measure the relatively small tilt anisoplanatism angles. The major conclusions of these measurements are given in the following paragraphs.

Tilt anisoplanatism is much greater than has been predicted by commonly used SLC models. It is a high-altitude phenomenon which can be modeled appropriately by increasing the free parameter in the Hufnagel-Valley atmospheric models for the refractive index structure function.

For a star separation of  $50 \mu\text{rad}$ , tilt anisoplanatism can typically be between  $0.5$  and  $1 \mu\text{rad}$  in each axis when using a  $1.2\text{-m-diam.}$  telescope aperture. The longitudinal component along the path separations is slightly larger than the lateral component. That ratio is somewhat lower than predicted by theory.

The measured data indicate that it is possible to predict tilt anisoplanatism magnitude from atmospheric coherence length and the isoplanatic angle. The isoplanatic angle affects the magnitude of tilt anisoplanatism more than the atmospheric coherence length.

While the shape of the power spectral density of tilt anisoplanatism measured of double stars is extremely variable, most energy lies at lower frequencies ( $<30 \text{ Hz}$ ) and is almost negligible above  $100 \text{ Hz}$ .

## ACKNOWLEDGMENTS

Since many individuals have been involved in the double-star measurements program, it would be impossible to single out every one who contributed to this work. Here we will recognize the contribution of some, other than the authors, who had significant impact on the project. We would first like to acknowledge the support, encouragement, and review of Leo Sullivan who was particularly instrumental in the overall system approach and the design and fabrication of the double-star measurement hardware. The subject of tilt anisoplanatism has been discussed with many individuals; among those willing to listen were: H. Praddaude, R. Sasiela, and R. Parenti of Lincoln Laboratory; R. Fugate and R. Cleis of the Air Force Weapons Laboratory; and G. Tyler, B. Ellerbroek, and D. Fried of the Optical Sciences Company. The Optical Sciences Co. team, under contract to Lincoln Laboratory, deserves special recognition for doing most of the numerical calculations which are given in this report and providing us with insight into the tilt anisoplanatism phenomenon. A. Dyer, H. Feinstein, J. Watson, E. Visconti, and M. Mattei participated heavily in the design, construction, and checkout of the double-star tracking hardware, and A. Ruscitti was instrumental in accomplishing data reduction.

## REFERENCES

1. D.L. Fried, "Anisoplanatism in Adaptive Optics," *J. Opt. Soc. Am.* **72**, 52 (1982).
2. D. Hoffleit, "Seeing," *Sky Telescope* **9**, 57 (1950).
3. J.H. DeWitt, R.H. Hardie, and C.K. Seyfert, "A Seeing Compensator Employing Television Techniques," *Sky Telescope* **17**, 8 (1957).
4. Editors Report, "American Astronomers Report," *Sky Telescope* **31**, 345 (1966).
5. L.J. Sullivan, "Infrared Coherent Radar," *CO<sub>2</sub> Laser Devices and Applications*, Proc. SPIE **227**, 148 (1980).
6. G.C. Loos and C.B. Hogge, "Turbulence of the Upper Atmosphere and Isoplanatism," *Appl. Opt.* **18**, 2654 (1979).
7. P. Couteau, *Observing Visual Double Stars* (MIT Press, Cambridge, MA, 1981).
8. R.E. Hufnagel, "Variations of Atmospheric Turbulence," Digest of Technical Papers, Topical Meeting on Optical Propagation Through Turbulence, Optical Society of America, Washington, DC, 1974.
9. B.L. Ellerbroek and P.H. Roberts, "Turbulence-Induced Angular Separation Measurement Errors: Expected Values for the SOR-2 Experiment," the Optical Sciences Co., Placentia, CA (December 1984), private communication.
10. F.D. Eaton, W.A. Peterson, J.R. Hines, and G. Fernandez, "Isoplanatic Angle Direct Measurements and Associated Atmospheric Conditions," *Appl. Opt.* **24**, 3264 (1985).
11. B.L. Ellerbroek, "The Measurement of Turbulence-Induced Wavefront Tilt Using a Nutating Quadrant Detector," the Optical Sciences Co., Placentia, CA, report in preparation.
12. B.L. Ellerbroek, "Measuring the Apparent Angular Separation of Binary Stars With a Pair of Quadrant Detectors," the Optical Sciences Co., Placentia, CA, report in preparation.
13. H.C. Praddaude, MIT Lincoln Laboratory, private communication.
14. R.J. Sasiela, MIT Lincoln Laboratory, private communication.

## REPORT DOCUMENTATION PAGE

1a. REPORT SECURITY CLASSIFICATION Unclassified		1b. RESTRICTIVE MARKINGS	
2a. SECURITY CLASSIFICATION AUTHORITY		3. DISTRIBUTION/AVAILABILITY OF REPORT Approved for public release; distribution unlimited.	
2b. DECLASSIFICATION/DOWNGRADING SCHEDULE			
4. PERFORMING ORGANIZATION REPORT NUMBER(S) Technical Report 815		5. MONITORING ORGANIZATION REPORT NUMBER(S) ESD-TR-88-203	
6a. NAME OF PERFORMING ORGANIZATION Lincoln Laboratory, MIT	6b. OFFICE SYMBOL (If applicable)	7a. NAME OF MONITORING ORGANIZATION Electronic Systems Division	
6c. ADDRESS (City, State, and Zip Code) P.O. Box 73 Lexington, MA 02173-0073		7b. ADDRESS (City, State, and Zip Code) Hanscom AFB, MA 01731	
8a. NAME OF FUNDING/SPONSORING ORGANIZATION Air Force Weapons Laboratory	8b. OFFICE SYMBOL (If applicable) AR-3	9. PROCUREMENT INSTRUMENT IDENTIFICATION NUMBER F19628-85-C-0002	
8c. ADDRESS (City, State, and Zip Code) Kirtland Air Force Base New Mexico 87117		10. SOURCE OF FUNDING NUMBERS	
		PROGRAM ELEMENT NO.	PROJECT NO. 268
		TASK NO.	WORK UNIT ACCESSION NO.
11. TITLE (Include Security Classification) Measurements of Tilt Anisoplanatism at the Firepond Facility			
12. PERSONAL AUTHOR(S) Rein Teoste; James A. Daley, Jr.; Raymond N. Capes, Jr.; Joseph J. Alves; Marvin D. Zimmerman; Alden V. Roberts			
13a. TYPE OF REPORT Technical Report	13b. TIME COVERED FROM _____ TO _____	14. DATE OF REPORT (Year, Month, Day) 1988, November, 18	15. PAGE COUNT 74
16. SUPPLEMENTARY NOTATION None			
17. COSATI CODES		18. SUBJECT TERMS (Continue on reverse if necessary and identify by block number)	
FIELD	GROUP	SUB-GROUP	tilt anisoplanatism; atmospheric measurements; Firepond Facility quad trackers; frequency distribution; binary stars; jitter, <i>l, h, d, e</i>
19. ABSTRACT (Continue on reverse if necessary and identify by block number)			
<p>➤ Tilt anisoplanatism is the atmosphere-induced differential tilt seen by a common telescope observing two light sources separated by a very small angle. This report summarizes the results of tilt anisoplanatism measurements made at the Firepond Facility in Westford, Massachusetts. Two very precise visible quad trackers were used to simultaneously track each component of selected binary stars whose angular separations were in the range of 47 to 107 <math>\mu</math>rad. While the report describes the tracking hardware and its characterization, the major contribution of this work is quantifying the tilt anisoplanatism under a variety of seeing conditions. The measurements showed that the magnitude of tilt anisoplanatism can be on the order of <math>1 \mu</math>rad rms for a 1.2-m telescope, a value several times larger than previously believed. The frequency distribution of the differential tilt is extremely variable, but most of the jitter strength lies below 30 Hz, with almost negligible contributions above 100 Hz. Calculations of the tilt anisoplanatism magnitude were made by the Optical Sciences Company using the SLC and Hufnagel-Valley turbulence models. The calculations are in general agreement with the measurements, but accurate predictions require precise atmospheric measurements as inputs to the models.</p>			
20. DISTRIBUTION/AVAILABILITY OF ABSTRACT <input type="checkbox"/> UNCLASSIFIED/UNLIMITED <input checked="" type="checkbox"/> SAME AS RPT. <input type="checkbox"/> DTIC USERS		21. ABSTRACT SECURITY CLASSIFICATION Unclassified	
22a. NAME OF RESPONSIBLE INDIVIDUAL Lt. Col. Hugh L. Southall, USAF	22b. TELEPHONE (Include Area Code) (617) 981-2330	22c. OFFICE SYMBOL ESD/TMI	